

Domains of pulsational instability of low–frequency modes in rotating upper main–sequence stars

Wojciech Szewczuk[★], Jadwiga Daszyńska–Daszkiewicz
Astronomical Institute of the Wrocław University, Kopernika 11, 51–622 Wrocław, Poland

Accepted XXX. Received YYY; in original form ZZZ

ABSTRACT

We determine instability domains on the Hertzsprung–Russel diagram for rotating main sequence stars with masses 2–20 M_{\odot} . The effects of the Coriolis force are treated in the framework of the traditional approximation. High–order g–modes with the harmonic degrees, ℓ , up to 4 and mixed gravity–Rossby modes with $|m|$ up to 4 are considered. Including the effects of rotation results in wider instability strips for a given ℓ comparing to the non–rotating case and in an extension of the pulsational instability to hotter and more massive models. We present results for the fixed value of the initial rotation velocity as well as for the fixed ratio of the angular rotation frequency to its critical value. Moreover, we check how the initial hydrogen abundance, metallicity, overshooting from the convective core and the opacity data affect the pulsational instability domains. The effect of rotation on the period spacing is also discussed.

Key words: stars: early–type – stars: oscillations – stars: rotation

1 INTRODUCTION

Two main classes of pulsating variables are usually distinguished amongst main sequence stars with masses $M \gtrsim 2.5 M_{\odot}$: β Cephei (Frost 1902; Stankov & Handler 2005) and Slowly Pulsating B–type stars (SPB, Waelkens 1991). The first class consists of early B–type stars with masses of 8–16 M_{\odot} and pulsate mainly in frequencies corresponding to low radial–order pressure and gravity (p and g) modes. The second class consists of stars of middle B spectral types pulsating with frequencies associated with high radial–order g modes. Pulsations of both types are driven in the metal (Z) opacity bump at $\log T \approx 5.3$ (Moskalik & Dziembowski 1992; Cox et al. 1992; Dziembowski et al. 1993; Gautschy & Saio 1993). However, this simple division into low–order p/g mode and high–order g mode pulsators is no longer valid. Recently, high–order g modes were detected in early B–type stars and low–order p/g modes, in mid B–type stars. First such hybrid pulsators were discovered from the ground (e.g. Jerzykiewicz et al. 2005; Handler et al. 2006; Chapellier et al. 2006). Subsequently, hybrid pulsators with far more rich oscillation spectra than those seen from the ground were discovered from space by projects such as MOST, CoRoT, Kepler and BRITE (Degroote et al. 2010; Balona et al. 2011; McNamara et al. 2012; Pápics et al. 2012, 2014, 2015; Balona et al. 2015; Pigulski et al. 2016). From the theoretical point of view, the important fact is that computations for non–

rotating models showed that g mode pulsations can be excited in very hot and massive stars (Pamyatnykh 1999). This result was obtained with both OPAL (Iglesias & Rogers 1996) and OP opacity tables (Seaton 1996).

The theoretical instability strip for g–mode pulsators has been constantly recomputed when the updated opacity data were released (e.g., Seaton 2005) or the new solar mixture was determined (Asplund et al. 2005, 2009). For example, Miglio et al. (2007b) and Zdravkov & Pamyatnykh (2008) investigated the influence of updated opacity data and chemical mixture on the SPB instability strip for non–rotating models and pulsational modes with $\ell = 1, 2$. Miglio et al. (2007a) extended the computations to $\ell = 3$.

Salmon et al. (2012) tested the effects of increasing the opacity in the region of the iron–group bump and of changing the chemical mixture on the excitation of pulsation modes in B–type stars in the Magellanic Clouds. Another example of this type of research are pulsational studies for massive stars by Cugier (2014) who identified a new opacity bump at $\log T = 5.06$ in the Kurucz stellar atmosphere models (Castelli & Kurucz 2003). Recently, Walczak et al. (2015) found that calculations with the new Los Alamos opacity data, OPLIB (Colgan et al. 2013, 2015), result in a wider SPB instability domain than those with OP or OPAL tables. Similarly, a wider instability strip was obtained by Moravveji (2016) who artificially enhanced the iron and nickel contribution to the Rosseland mean opacity by 75 %. This was motivated by the work of Bailey et al. (2015) who reported higher than predicted laboratory measurement of iron opac-

[★] E-mail: szewczuk@astro.uni.wroc.pl (WS)

ity at solar interior temperatures. Laboratory measurements and theoretical computations of iron and nickel opacities for envelopes of massive stars were also performed by [Turck-Chièze et al. \(2013\)](#) who concluded that a significant increase in comparison with the OP data is predicted for the nickel opacity.

The instability domains of gravity modes with the effects of rotation on pulsations taken into account have been computed by [Townsend \(2005a,b\)](#). His calculations were carried out in the so-called traditional approximation and all effects of rotation on the evolutionary models were omitted; the chemical mixture of [Grevesse & Noels \(1993, GN93\)](#) was used. This author considered $\ell \leq 2$ g modes for models with masses smaller than $13 M_{\odot}$ ([Townsend 2005a](#)) and mixed gravity–Rossby modes for models with masses smaller than $8 M_{\odot}$ ([Townsend 2005b](#)).

Here we extend Townsend’s computations to the harmonic degree up to $\ell = 4$ and $|m| \leq \ell$ as well as mixed gravity–Rossby modes, also known as r modes, with $|m| \leq 4$ ([Lee 2006](#); [Daszynska-Daszkiewicz et al. 2007](#)) for models with masses $2 - 20 M_{\odot}$. Including higher ℓ and r modes was motivated by the high precision space-based photometry. Furthermore, the most recent chemical mixture of [Asplund et al. \(2009\)](#) was used in our calculations. In the present paper by SPB modes we mean high radial-order g modes.

In Section 2, we present instability strips for our reference rotating models with masses in the range $2 - 20 M_{\odot}$. In Section 3, the effects of the initial hydrogen abundance, metallicity, core overshooting and the opacity data on the SPB instability strip are discussed. Section 4 is devoted to checking the impact on the instability strip of using a fixed ratio of the angular rotation frequency to its critical value instead of a fixed equatorial velocity. The influence of rotation on the period spacing for high radial-order g modes is examined in Section 5. We end with a summary in Section 6.

2 LOW-FREQUENCY MODES IN ROTATING MODELS OF UPPER MAIN SEQUENCE STARS

In the present paper we will consider only low-frequency (slow) modes, i.e., high-order gravity as well as mixed gravity–Rossby modes. The latter become propagative in the radiative envelope only if the rotation is fast enough (e.g., [Savonije 2005](#); [Townsend 2005b](#)). Low radial-order p and g modes which can be also excited in B-type stars and are responsible for β Cephei phenomenon are omitted here.

Since the periods of the slow modes are often of the order of the rotation period, the effects of rotation cannot be regarded as a small perturbation to the pulsations another treatment is needed. In particular, the effects of the Coriolis force have to be taken into account. As far as the centrifugal force is concerned, [Ballot et al. \(2012, 2013\)](#) showed that its effects on g modes can be safely neglected if the rotation rate is well below the critical value. In the first paper these authors used the condition $\Omega < 0.7\Omega_{\text{crit}}$ where Ω and Ω_{crit} are the angular frequency of rotation and its critical value, respectively, but they did not justify their choice. Moreover, in the second paper ([Ballot et al. 2013](#)) they mentioned that an impact of the centrifugal force is negligible

below a lower threshold $\Omega < 0.4\Omega_{\text{crit}}$ and it affects mostly prograde sectoral modes ($\ell = m$). In the present paper, following [Townsend \(2005a\)](#), [Dziembowski et al. \(2007\)](#) and [Daszyńska-Daszkiewicz et al. \(2015\)](#), as an upper limit of the applicability of the traditional approximation, we used a less rigorous condition, i.e., $\Omega \lesssim 0.7\Omega_{\text{crit}}$ corresponding to the value of [Ballot et al. \(2012\)](#).

While including the effects of Coriolis force one often adopts the traditional approximation (e.g., [Lee & Saio 1997](#); [Townsend 2003a,b, 2005a,b](#); [Dziembowski et al. 2007](#); [Daszynska-Daszkiewicz et al. 2007](#)) or a truncated expansion in the associated Legendre polynomials for the eigenfunctions (e.g., [Lee & Saio 1989](#); [Lee 2001](#)). In the present paper we will use the first approach in which the horizontal component of the Coriolis force related to the radial motion and the radial component of the Coriolis force related to the horizontal motion are neglected (e.g., [Townsend 2003a](#)).

Here, we computed evolutionary models with the Warsaw–New Jersey code (e.g. [Pamyatnykh et al. 1998](#)). In this code, a very simple approach of including rotation is used, i.e., the effect of the averaged centrifugal force is taken into account in the equation of hydrostatic equilibrium. The rotation is assumed uniform and the global angular momentum is conserved during the evolution.

2.1 Instability domains of high-order g modes

We constructed a grid of evolutionary models with masses ranging from 2 to $20 M_{\odot}$ and with steps: $0.05 M_{\odot}$ for $M \leq 3.5 M_{\odot}$, $0.1 M_{\odot}$ for $3.5 M_{\odot} < M \leq 12.2 M_{\odot}$, $0.2 M_{\odot}$ for $12.2 M_{\odot} < M \leq 14 M_{\odot}$, and $0.5 M_{\odot}$ for $M > 14 M_{\odot}$. As a reference set of parameters, we chose the initial hydrogen abundance, $X_0 = 0.7$, metallicity, $Z = 0.015$, and no overshooting from the convective core, $\alpha_{\text{ov}} = 0.0$. We used the OP opacity tables ([Seaton 2005](#)) and the AGSS09 chemical mixture ([Asplund et al. 2009](#)). At lower temperatures, $\log T < 3.95$, the opacities were supplemented with the [Ferguson et al. \(2005\)](#) data. We adopted OPAL equation of state ([Rogers & Nayfonov 2002](#)) and the nuclear reaction rates from [Bahcall et al. \(1995\)](#). In the envelope, convection was treated in the framework of the standard mixing-length theory (MLT) with the parameter $\alpha_{\text{MLT}} = 1.0$. The value of α_{MLT} does not affect the pulsational computations for masses considered in this paper. Three values of the rotation velocity on the Zero Age Main Sequence (ZAMS) were assumed, $V_{\text{rot}} = 0, 100$ and 200 km s^{-1} . The last value was chosen because it is more or less the upper limit of the applicability of the traditional approximation as well as because most B-type stars rotate with equatorial velocity below or around 200 km s^{-1} (see e.g. [Huang & Gies 2006](#)). We have to add that at $V_{\text{rot}} = 200 \text{ km s}^{-1}$ a small number of low mass models close to Terminal Age Main Sequence (TAMS) has Ω slightly exceeding $0.7\Omega_{\text{crit}}$ (see Fig. A1 in Appendix A), but this fact does not spoil the overall picture of our results. Nevertheless, the computed mode frequencies and instabilities have to be treated with some caution, especially for the prograde sectoral modes which are mostly affected by the centrifugal force. It should also be kept in mind that fast rotation can stabilize retrograde g modes if a truncated expansion of the Legendre functions for the eigenfunctions is used ([Lee 2008](#); [Aprilia et al. 2011](#)). The ranges of $\Omega/\Omega_{\text{crit}}$, corresponding to fixed values of equatorial velocities for models in a given

instability strip are listed in the last columns of Tables 1, 3 and 4.

Linear nonadiabatic pulsational calculations were done with the Dziembowski code in its version which includes the effects of rotation in the traditional approximation (Dziembowski et al. 2007). This code uses the same approach as that adopted by Townsend (2005a). Moreover, the freezing approximation is assumed for the convective flux; this is fully justified for the range of masses we consider.

For all models from ZAMS to TAMS, the pulsations were computed for the rotation velocities fixed to the ZAMS values, i. e., for $V_{\text{rot,MS}} = V_{\text{rot,ZAMS}} = 0, 100$ and 200 km s^{-1} . We considered high-order g modes with the spherical harmonic degrees, $\ell \leq 4$, and azimuthal orders, $-\ell \leq m \leq \ell$, with the convention $m > 0$ for prograde modes.

One of the important assumptions in the traditional approximation is that of a small contribution of the horizontal heat losses to the overall work integral. This is because replacing the eigenvalue $\ell(\ell+1)$ by λ does not correctly include these losses which are proportional to the mode degree (cf. Townsend 2005a; Dziembowski et al. 2007). Here we consider modes up to $\ell = 4$, thus, it is interesting to check whether neglecting the horizontal heat losses is valid for such high degree modes. In Fig. 1, we plot the differential work integral for high-order g modes with $\ell = 4$ considering two models with masses typical for SPB and β Cephei stars: 5 and $10 M_{\odot}$, respectively. The corresponding effective temperatures of these models are $\log T = 4.2098$ and $\log T = 4.3565$, respectively. The work integral was computed with the zero-rotation approximation. In addition, in Fig. 1 we marked the instability parameter η for both modes. The parameter η is the normalized total work integral and modes which are pulsational unstable have positive values of η . As one can see, the horizontal heat losses are negligible and have the largest contribution below the Z-bump ($\log T < 5.3$). One can also see that the effect of the horizontal heat losses slightly increases with mass.

The instability strip of the dipole modes on the Hertzsprung–Russel (H–R) diagram is shown in Fig. 2. In the case of retrograde and axisymmetric modes, rotation shifts the whole instability domains towards higher masses and effective temperatures and makes the instability domains wider. For prograde sectoral modes the shift caused by rotation is reversed. Moreover, for $V_{\text{rot}} = 200 \text{ km s}^{-1}$ and dipole modes with $m = 0, -1$, the instability extends beyond the mass range considered in our grid. For retrograde modes ($\ell = 1, m = -1$) and $V_{\text{rot}} = 100 \text{ km s}^{-1}$, the instability ends at $M = 13 M_{\odot}$ and appears again at the edge of our grid for $M = 20 M_{\odot}$.

The boundary values of masses, M , effective temperatures, $\log T_{\text{eff}}$, luminosities, $\log L/\log L_{\odot}$, and gravities, $\log g$, for instability domains for our reference models with ℓ up to 4, $|m| \leq \ell$ and $V_{\text{rot}} = 0, 100$ and 200 km s^{-1} are summarized in Table 1.

In the non-rotating models, increasing ℓ shifts the instability strip to higher masses and higher effective temperatures. This behaviour can be seen easily when we compare Fig. 2 with Fig. 3 or 4 where the instability strips for dipole and quadrupole modes are shown, respectively. The instability strips for modes with $\ell = 3$ and 4 are presented in Appendix B (Figs. B1–B6). For modes with $\ell \geq 2$ we did not find upper boundaries of the mass and effective temperature within the considered grid of models. An exception are the

modes (2, +2) at $V_{\text{rot}} = 100 \text{ km s}^{-1}$. In this case there is a gap in the instability strip, i. e. models with masses between 14 and $17 M_{\odot}$ are pulsationally stable during their whole main-sequence evolution.

It should be mentioned that the location of TAMS and consequently our instability borders are sensitive to the amount of overshooting from the convective core. Including overshooting prolongs the main sequence stage and extends instability to higher luminosities. This effect is investigated in Section 3.

When the effects of rotation are taken into account, increasing of V_{rot} acts in the same direction as increasing of the mode degree ℓ . The exception are the prograde sectoral modes, $\ell = m$, for which the instability strip is shifted toward lower masses and effective temperatures, as discussed for dipole $m = 1$ modes (see Fig. 2). This behaviour is connected with the eigenvalue λ which is a counterpart of the eigenvalue $\ell(\ell+1)$ in the non-rotating case (e. g. Dziembowski et al. 2007; Daszyńska-Daszkiewicz et al. 2008). Let us remind the reader that in the traditional approximation the latitudinal relationships are described by the Hough functions $\Theta_{\lambda}^m(\theta)$ which are the solutions of the tidal Laplace equation for a given eigenvalue λ . For all modes but the prograde sectoral ones, the value of λ is a monotonically increasing function of the spin parameter, s , defined as the doubled ratio of the rotation angular frequency to the pulsation frequency in the co-rotating frame, $s = 2\Omega/\omega$. In the case of the prograde sectoral modes, λ slowly decreases with increasing s , or with the rotation rate at a fixed value of the pulsation frequency and tends to an asymptotic value. The behaviour of λ has an impact on the behaviour of eigenfrequencies and has implications for the instability of different modes. Therefore prograde sectoral modes are less sensitive to the rotation velocity than other pulsational modes. An exact explanation of the instability properties of prograde sectoral and other modes was given by Townsend (2005a).

2.2 Impact of rotation on the range of unstable frequencies

Now, let us discuss the values of the frequencies of excited modes. In Figs. 2–4 and Figs. B1–B6, we coded in colours the observer’s frame frequencies of the most unstable modes, i. e., the modes for which the instability parameter η reaches maximum. If not stated otherwise, the frequencies in the inertial frame are used throughout the paper.

The mode frequencies at the maximum of η can be treated as a kind of a mean frequency of unstable modes in a given model for specified angular indices (ℓ, m), i. e. these modes are more or less in the middle of frequency range of unstable modes. Sometimes, especially on the border of the instability domains, there is only one unstable mode. However, more often there are many unstable modes. Examples of the evolution of frequencies and their ranges for dipole modes excited in models with masses $4, 6$, and $9 M_{\odot}$ are presented in Appendix C, Figs. C1–C3. In Fig. C4 the evolution of the frequencies of $\ell = 2-4$ modes for non-rotating, and $\ell = 2$ for rotating $4 M_{\odot}$ models is shown.

As was mentioned above, for a given model, there are many unstable modes with the same angular indices (ℓ, m). Therefore, in the penultimate column of Table 1, there were given frequency ranges of all unstable modes. Of course,

Table 1. The ranges of mass, effective temperature, luminosity and surface gravity for the instability domains of the reference models with $V_{\text{rot}} = 0, 100, 200 \text{ km s}^{-1}$. Results for all pulsational modes with $\ell = 1 - 4$ are shown. Note that in the non-rotating case, modes are degenerated in the azimuthal order m . The asterisk indicates the limit of the model grid rather than the limit of the instability domain. In the penultimate column there is given the range of frequencies of all unstable modes (in the observer frame). Frequencies of „reflected” modes, i.e. those which formally have the negative values of frequencies, are given in parentheses. In the last column the ranges of the ratio of angular rotation rate to its critical value for models within the given instability domain are listed.

Grid	V_{rot} [km s^{-1}]	mode (ℓ, m)	M [M_{\odot}]	$\log T_{\text{eff}}$	$\log L/L_{\odot}$	$\log g$	ν [d^{-1}]	$\Omega/\Omega_{\text{crit}}$
0		(1)	2.75 – 9.10	4.032 – 4.305	1.77 – 3.90	3.67 – 4.36	0.2162 – 1.6026	0.00
		(2)	3.00 – 20.00*	4.060 – 4.437*	1.91 – 4.95*	3.45* – 4.36	0.3206 – 2.6318	0.00
		(3)	3.15 – 20.00*	4.080 – 4.456*	1.99 – 4.95*	3.45* – 4.36	0.4101 – 3.5454	0.00
		(4)	3.30 – 20.00*	4.095 – 4.469*	2.07 – 4.95*	3.45* – 4.36	0.4929 – 2.3470	0.00
100		(1, –1)	3.00 – 13.00	4.066 – 4.371	1.91 – 4.41	3.57 – 4.34	0.0991 – 1.3095	0.28 – 0.44
		(1, –1)	20.00* – 20.00*	4.425* – 4.425*	4.95* – 4.95*	3.43* – 3.43*	0.2178 – 0.2327	0.35 – 0.35
		(1, +0)	2.85 – 10.30	4.046 – 4.328	1.83 – 4.08	3.63 – 4.34	0.3174 – 1.7661	0.29 – 0.45
		(1, +1)	2.65 – 8.20	4.019 – 4.280	1.71 – 3.74	3.67 – 4.34	0.5429 – 2.3164	0.29 – 0.46
		(2, –2)	3.10 – 20.00*	4.076 – 4.445*	1.97 – 4.95*	3.43* – 4.34	(0.3607) – 1.2483	0.27 – 0.44
		(2, –1)	3.15 – 20.00*	4.081 – 4.445*	1.99 – 4.95*	3.43* – 4.34	0.2094 – 2.0576	0.27 – 0.44
		(2, +0)	3.10 – 20.00*	4.074 – 4.442*	1.97 – 4.95*	3.43* – 4.34	0.4036 – 2.7899	0.28 – 0.44
		(2, +1)	3.05 – 20.00*	4.065 – 4.438*	1.94 – 4.95*	3.43* – 4.34	0.5296 – 3.5429	0.28 – 0.45
		(2, +2)	2.95 – 14.00	4.053 – 4.383	1.88 – 4.50	3.56 – 4.34	0.8523 – 4.2689	0.28 – 0.45
		(2, +2)	17.00 – 20.00*	4.409 – 4.433*	4.75 – 4.95*	3.43* – 3.50	0.6533 – 0.7864	0.34 – 0.35
		(3, –3)	3.25 – 20.00*	4.089 – 4.460*	2.04 – 4.95*	3.43* – 4.34	(1.0289) – 1.3043	0.27 – 0.44
		(3, –2)	3.30 – 20.00*	4.092 – 4.460*	2.07 – 4.95*	3.43* – 4.34	(0.1497) – 2.0969	0.27 – 0.44
		(3, –1)	3.30 – 20.00*	4.093 – 4.460*	2.07 – 4.95*	3.43* – 4.34	0.2817 – 2.8573	0.27 – 0.44
		(3, +0)	3.25 – 20.00*	4.090 – 4.459*	2.04 – 4.95*	3.43* – 4.34	0.4778 – 3.6251	0.27 – 0.44
		(3, +1)	3.25 – 20.00*	4.086 – 4.458*	2.04 – 4.95*	3.43* – 4.34	0.6087 – 4.4622	0.27 – 0.44
		(3, +2)	3.20 – 20.00*	4.082 – 4.456*	2.02 – 4.95*	3.43* – 4.34	0.7315 – 5.2454	0.27 – 0.44
		(3, +3)	3.15 – 20.00*	4.075 – 4.455*	1.99 – 4.95*	3.43* – 4.34	0.8657 – 6.0119	0.27 – 0.44
		(4, –4)	3.40 – 20.00*	4.102 – 4.471*	2.12 – 4.95*	3.43* – 4.34	(1.6677) – 1.3370	0.27 – 0.43
		(4, –3)	3.40 – 20.00*	4.104 – 4.472*	2.12 – 4.95*	3.43* – 4.34	(0.7022) – 2.0928	0.27 – 0.43
		(4, –2)	3.40 – 20.00*	4.105 – 4.471*	2.12 – 4.95*	3.43* – 4.34	(0.0529) – 2.8552	0.27 – 0.43
	(4, –1)	3.40 – 20.00*	4.105 – 4.471*	2.12 – 4.95*	3.43* – 4.34	0.3346 – 3.6039	0.27 – 0.43	
	(4, +0)	3.40 – 20.00*	4.103 – 4.471*	2.12 – 4.95*	3.43* – 4.34	0.5493 – 4.4406	0.27 – 0.43	
	(4, +1)	3.40 – 20.00*	4.102 – 4.471*	2.12 – 4.95*	3.43* – 4.34	0.6787 – 5.2348	0.27 – 0.43	
	(4, +2)	3.35 – 20.00*	4.099 – 4.469*	2.09 – 4.95*	3.43* – 4.34	0.8146 – 6.0251	0.27 – 0.43	
	(4, +3)	3.35 – 20.00*	4.096 – 4.469*	2.09 – 4.95*	3.43* – 4.34	0.9455 – 6.8330	0.27 – 0.44	
	(4, +4)	3.30 – 20.00*	4.091 – 4.468*	2.07 – 4.95*	3.43* – 4.34	1.0731 – 7.6288	0.27 – 0.44	
200		(1, –1)	3.30 – 20.00*	4.089 – 4.447*	2.06 – 4.94*	3.35* – 4.28	(0.0919) – 1.2089	0.53 – 0.83
		(1, +0)	3.00 – 20.00*	4.059 – 4.425*	1.90 – 4.94*	3.35* – 4.28	0.2997 – 2.0555	0.55 – 0.85
		(1, +1)	2.65 – 8.60	4.014 – 4.282	1.70 – 3.81	3.60 – 4.28	0.7865 – 3.1563	0.57 – 0.88
		(2, –2)	3.35 – 20.00*	4.093 – 4.456*	2.08 – 4.94*	3.35* – 4.28	(1.5798) – 0.1472	0.53 – 0.83
		(2, –1)	3.45 – 20.00*	4.107 – 4.460*	2.13 – 4.94*	3.35* – 4.28	0.0700 – 1.8633	0.52 – 0.83
		(2, +0)	3.30 – 20.00*	4.092 – 4.455*	2.06 – 4.94*	3.35* – 4.28	0.4238 – 3.1703	0.53 – 0.83
		(2, +1)	3.15 – 20.00*	4.073 – 4.446*	1.98 – 4.94*	3.35* – 4.28	0.6247 – 4.5348	0.54 – 0.84
		(2, +2)	2.95 – 20.00*	4.049 – 4.435*	1.88 – 4.94*	3.35* – 4.28	0.8393 – 5.9309	0.55 – 0.86
		(3, –3)	3.40 – 20.00*	4.100 – 4.467*	2.11 – 4.94*	3.35* – 4.28	(3.1684) – (0.0175)	0.52 – 0.83
		(3, –2)	3.50 – 20.00*	4.111 – 4.468*	2.16 – 4.94*	3.35* – 4.28	(1.1147) – 0.9181	0.52 – 0.82
		(3, –1)	3.60 – 20.00*	4.119 – 4.469*	2.20 – 4.94*	3.35* – 4.28	0.1859 – 2.4609	0.52 – 0.82
		(3, +0)	3.50 – 20.00*	4.109 – 4.467*	2.16 – 4.94*	3.35* – 4.28	0.5110 – 3.9127	0.52 – 0.82
		(3, +1)	3.40 – 20.00*	4.099 – 4.464*	2.11 – 4.94*	3.35* – 4.28	0.7335 – 5.4101	0.52 – 0.83
		(3, +2)	3.30 – 20.00*	4.086 – 4.461*	2.06 – 4.94*	3.35* – 4.28	0.9571 – 6.9289	0.53 – 0.84
		(3, +3)	3.15 – 20.00*	4.071 – 4.456*	1.98 – 4.94*	3.35* – 4.28	1.1772 – 8.5067	0.53 – 0.85
		(4, –4)	3.60 – 20.00*	4.109 – 4.475*	2.20 – 4.94*	3.35* – 4.28	(4.6932) – (0.1415)	0.52 – 0.82
		(4, –3)	3.60 – 20.00*	4.117 – 4.476*	2.20 – 4.94*	3.35* – 4.28	(2.6540) – 0.1937	0.51 – 0.82
		(4, –2)	3.70 – 20.00*	4.123 – 4.476*	2.24 – 4.94*	3.35* – 4.28	(0.7842) – 1.6143	0.51 – 0.82
		(4, –1)	3.70 – 20.00*	4.127 – 4.476*	2.24 – 4.94*	3.35* – 4.28	0.2784 – 3.0516	0.51 – 0.81
		(4, +0)	3.70 – 20.00*	4.122 – 4.476*	2.24 – 4.94*	3.35* – 4.28	0.6091 – 4.5461	0.51 – 0.82
	(4, +1)	3.60 – 20.00*	4.116 – 4.475*	2.20 – 4.94*	3.35* – 4.28	0.8347 – 6.1004	0.52 – 0.82	
	(4, +2)	3.50 – 20.00*	4.109 – 4.474*	2.16 – 4.94*	3.35* – 4.28	1.0480 – 7.6309	0.52 – 0.82	
	(4, +3)	3.45 – 20.00*	4.099 – 4.472*	2.13 – 4.94*	3.35* – 4.28	1.2823 – 9.2755	0.52 – 0.83	
	(4, +4)	3.35 – 20.00*	4.089 – 4.469*	2.08 – 4.94*	3.35* – 4.28	1.5098 – 10.8095	0.52 – 0.83	

 OP $X_0 = 0.70$ $Z = 0.015$ $\alpha_{\text{ov}} = 0.0$

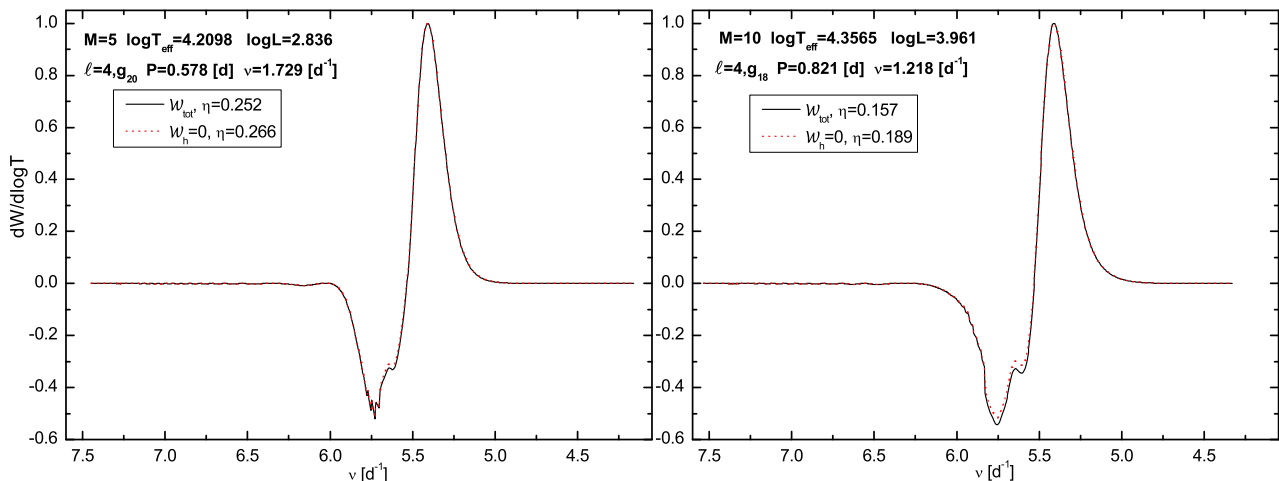


Figure 1. The run of the differential work integral, $\mathcal{W} = dW/d \log T$, inside the models of $5 M_{\odot}$ (the left panel) and $10 M_{\odot}$ (the right panel) for unstable high-order g modes with the degree $\ell = 4$. Models were computed with the OP opacities for $X_0 = 0.7$, $Z = 0.015$, $\alpha_{\text{ov}} = 0$ and the AGSS09 chemical mixture. The dotted lines indicate the work integrals without the horizontal losses. The values of the normalized instability parameter, η , are given in the insets. Both modes are unstable.

these ranges are much wider than the ranges of frequencies at the maximum η presented in the figures.

The range of the excited frequencies is a function of many variables. Here, we discuss some of them. Firstly, the frequencies of the excited modes depend on the model parameters. Generally, the less evolved the model the higher frequencies are excited. Moreover, for the close-to-ZAMS models the frequency values increase with decreasing mass. This behaviour is the consequence of the sensitivity of the frequency of excited modes to the location of the driving region. However, we would like to stress that there are exceptions to this trend: the most important is that the reflected modes obey it in the corotating frame only (see below). Secondly, unstable modes with higher ℓ have higher frequencies. Thirdly, rotation has a profound impact on the frequency values. With the increasing rotation rate, modes with the same ℓ but different m can have very different frequencies in the observer’s frame. We would like to emphasize that for some of our prograde sectoral modes with $\ell = 4$ rotation can shift unstable g modes to very high frequencies (e.g., $\nu \approx 10 \text{ d}^{-1}$) which are typically not associated with the SPB variables. Moreover, for the higher rotation rates, the retrograde modes can be reflected, i.e., they have frequencies smaller than rotation frequency and in the observer’s frame they have formally negative values, whereas they are observed as prograde modes. Examples are the $(4, -4)$ modes at $V_{\text{rot}} = 200 \text{ km s}^{-1}$.

Furthermore, in the case of the axisymmetric modes, increasing the rotation velocity acts in the same direction as increasing the mode degree. The frequencies of the $m = 0$ modes with the same ℓ become higher as V_{rot} increases. For these modes we have a pure effect of the Coriolis force. In the case of the sectoral prograde modes, mainly the Doppler effects is seen because their eigenvalues λ change very slightly with rotation (e.g., Daszyńska-Daszkiewicz et al. 2015).

In Table 2, we give the ranges of the radial orders and frequencies of unstable modes for a few selected models with masses 4 and $9 M_{\odot}$. In general, for all modes but the sectoral prograde ones, for higher rotation rates we have more pul-

sational modes in a given frequency range. However, their stability conditions depend on the particular model.

2.3 Instability domains of mixed gravity–Rossby modes

Mixed gravity–Rossby (r) modes are retrograde ones with $m = -\ell$. They may be excited and visible in the light variations if rotation is fast enough (Savonije 2005; Townsend 2005b). For these modes, the restoring forces are both buoyancy and Coriolis force as compared with the sole buoyancy force in the case of gravity modes. The r modes in the considered models are driven by the κ -mechanism operating in the same Z-bump layer as in the case of gravity modes.

As far as observations are concerned, Walker et al. (2005) suggested that some frequency peaks detected in HD 163868 in the MOST data may be identified as r modes. However, Dziembowski et al. (2007) showed that the whole oscillation spectrum of the star can be explained solely by g modes. Subsequently, Szewczuk & Daszyńska-Daszkiewicz (2015) carried out mode identification for 31 SPB stars with available multicolour ground-based photometry and found that scarcely two frequencies observed in two stars may be associated, but with rather low probability, with r modes. Nevertheless, we think that in the era of high-precision space photometry, detection of r modes is only a question of time, hence the motivation to consider them.

We computed the r mode instability strips for $m = -1, -2, -3$ and -4 for the reference models described in the previous subsection. The results are presented in Fig. 5 (for $m = -1$ and -2) as well as in Fig. B7 (for $m = -3$ and -4), and are summarised in Table 3.

The first important finding is that with increasing rotation velocity, from $V_{\text{rot}} = 100 \text{ km s}^{-1}$ to 200 km s^{-1} , the instability strip of the r -modes for a given m expands and is shifted towards higher masses and effective temperatures. The second conclusion is that if we go towards more negative values of m , the instability strip shrinks and moves towards lower masses and effective temperatures. In the case

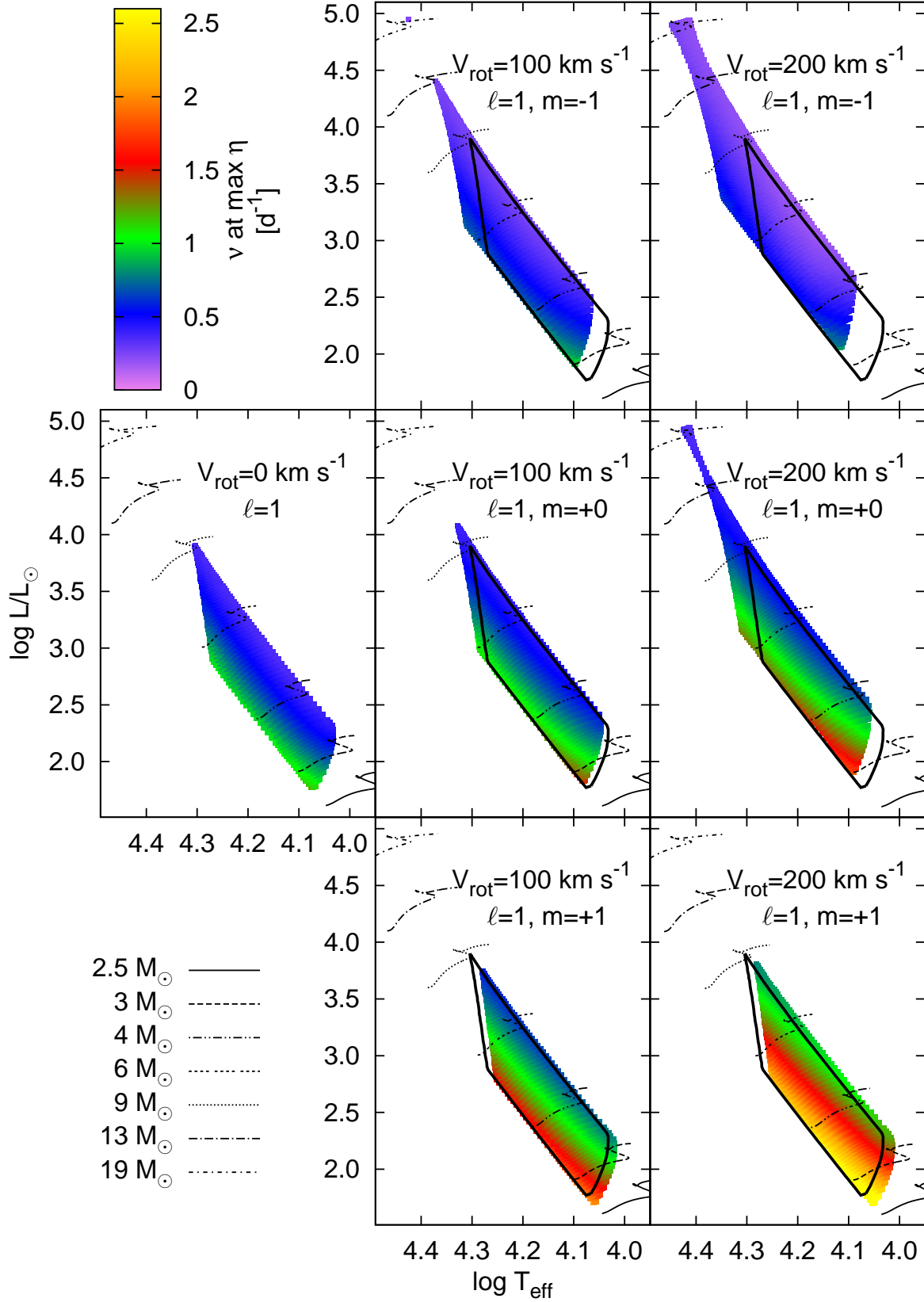


Figure 2. The SPB instability strip on the H-R diagram. There are shown the dipole modes with all possible azimuthal orders. Models were computed with the OP opacity tables assuming $X_0 = 0.7$, $Z = 0.015$, $\alpha_{\text{ov}} = 0$ and three values of the rotation velocity, $V_{\text{rot}} = 0$, 100 and 200 km s^{-1} . Colours code the values of the mode frequency in the inertial frame at which the instability parameter, η , reaches maximum. There are also shown the evolutionary tracks for 2.5 , 3 , 4 , 6 , 9 , 13 and $19 M_{\odot}$. For a better comparison, the instability domain for the non-rotating case is additionally marked on the panels with the rotating models with thick black lines. (Colour figure only in the electronic edition of the journal.)

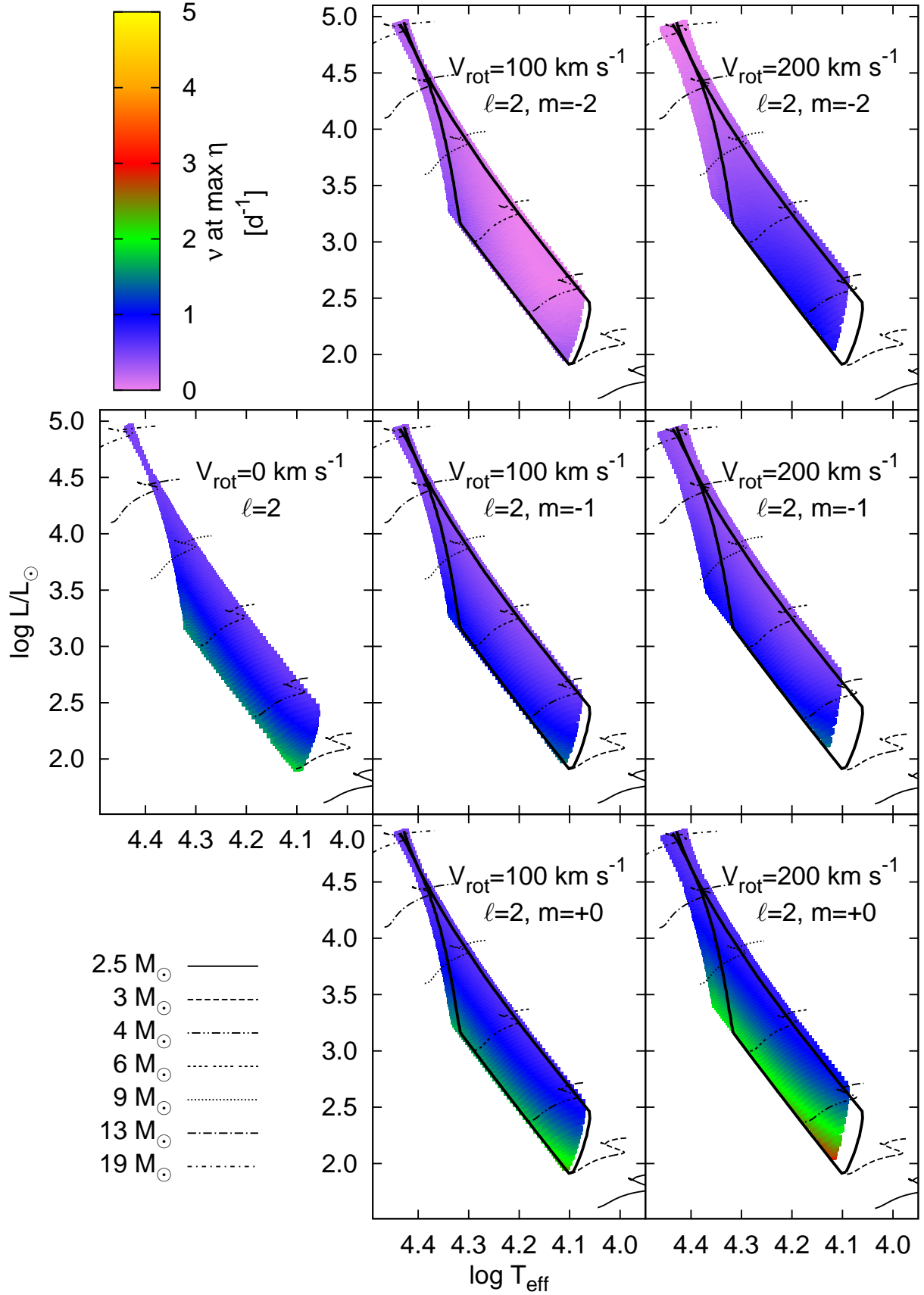


Figure 3. The same as in Fig. 2 but for modes with $\ell = 2$ and $m \leq 0$.

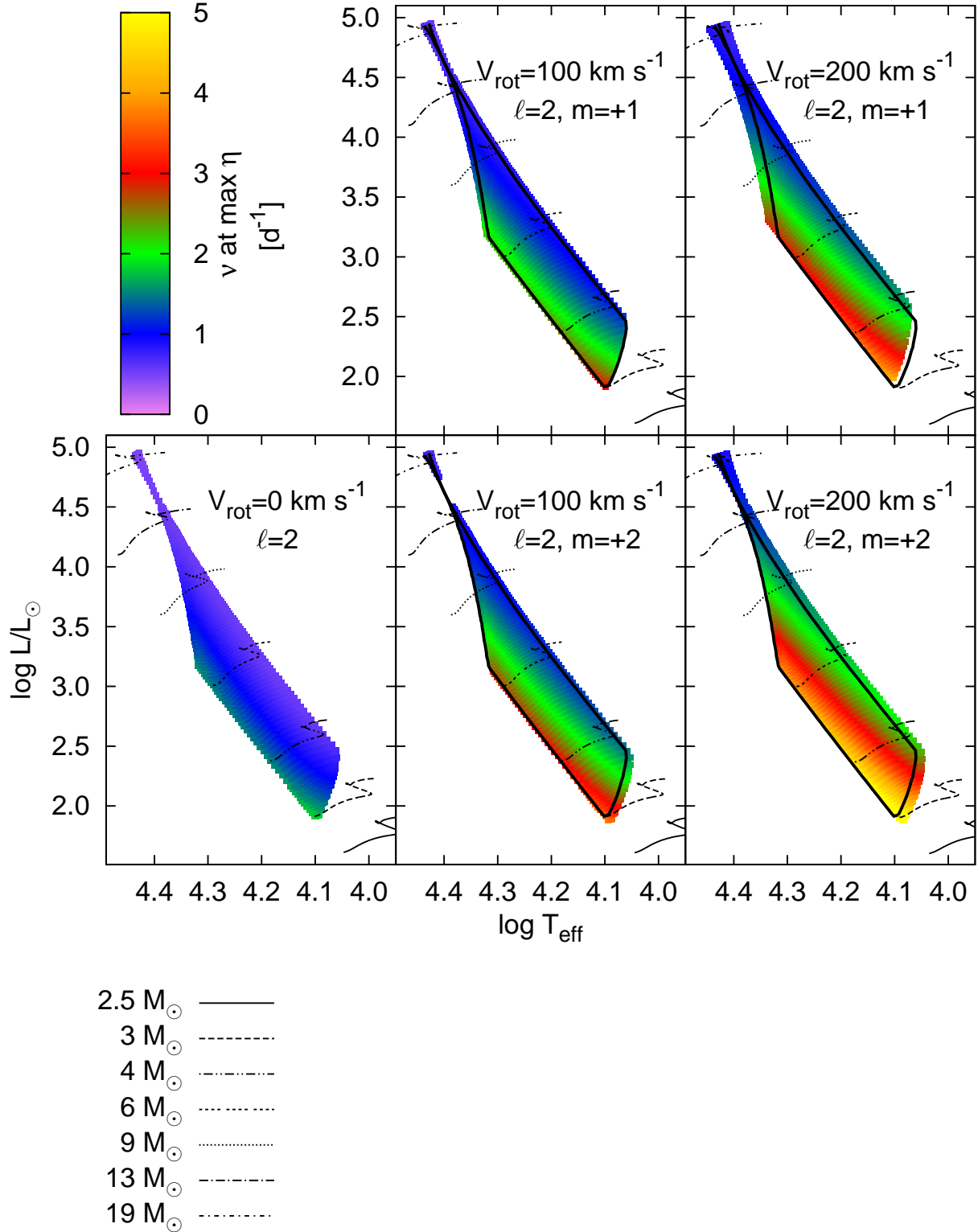


Figure 4. The same as in Fig. 2 but for modes with $\ell = 2$ and $m \geq +1$.

Table 2. The instability ranges for the g modes in the models near ZAMS ($X_c = 0.65$), in the middle of the main-sequence evolution ($X_c = 0.35$) and near TAMS ($X_c = 0.10$) for two stellar masses, $M = 4$ and $9 M_\odot$. Three values of the rotation velocity are considered, $V_{\text{rot}} = 0, 100$ and 200 km s^{-1} . For each (ℓ, m) pair, the range of radial orders, n , and frequencies in the observer frame, ν , spanned by the unstable modes is listed (formally negative values for reflected modes are given in parentheses).

$M [M_\odot]$	$V_{\text{rot}} [\text{km s}^{-1}]$	(ℓ, m)	$X_c = 0.65$		$X_c = 0.35$		$X_c = 0.10$		
			n	$\nu [\text{d}^{-1}]$	n	$\nu [\text{d}^{-1}]$	n	$\nu [\text{d}^{-1}]$	
4	0	(1)	21 – 9	0.6005 – 1.3448	39 – 14	0.3586 – 0.9588	71 – 28	0.2397 – 0.5967	
		(2)	24 – 9	0.9176 – 2.3130	44 – 15	0.5508 – 1.5505	72 – 30	0.4091 – 0.9649	
	100	(1, -1)	26 – 8	0.3846 – 1.1399	44 – 14	0.2396 – 0.7616	59 – 29	0.2339 – 0.4731	
		(1, +0)	23 – 8	0.8161 – 1.5202	43 – 14	0.5336 – 1.0354	71 – 28	0.4002 – 0.6927	
		(1, +1)	18 – 8	1.3222 – 1.9226	35 – 14	0.8865 – 1.3267	67 – 27	0.6375 – 0.9293	
		(2, -2)	26 – 8	(0.3388) – 1.0396	44 – 15	(0.3024) – 0.5381	55 – 32	(0.1240) – 0.2000	
		(2, -1)	27 – 8	0.6657 – 1.8619	42 – 15	0.4728 – 1.1538	49 – 33	0.4714 – 0.6710	
		(2, +0)	26 – 8	1.2692 – 2.5410	44 – 15	0.8732 – 1.6416	56 – 31	0.7498 – 1.0735	
		(2, +1)	25 – 8	1.8392 – 3.1646	44 – 15	1.2665 – 2.0865	65 – 30	0.9934 – 1.4278	
		(2, +2)	23 – 8	2.4286 – 3.7593	42 – 15	1.6725 – 2.5109	73 – 29	1.2426 – 1.7716	
	200	(1, -1)	27 – 9	0.1034 – 1.0280	38 – 17	0.1203 – 0.6279	–	–	
		(1, +0)	27 – 8	1.0325 – 1.8549	46 – 15	0.7053 – 1.2313	60 – 32	0.5949 – 0.8200	
		(1, +1)	19 – 8	2.0549 – 2.6284	38 – 14	1.4118 – 1.8385	72 – 28	1.0379 – 1.3044	
		(2, -2)	27 – 9	(1.4572) – (0.2283)	37 – 18	(0.9846) – (0.4108)	–	–	
		(2, -1)	25 – 10	0.6510 – 1.5472	30 – 19	0.6447 – 0.9755	–	–	
		(2, +0)	27 – 9	1.7391 – 2.8637	37 – 18	1.3211 – 1.8475	–	–	
		(2, +1)	28 – 9	2.7910 – 3.9632	44 – 16	2.0001 – 2.7406	50 – 36	1.6660 – 1.8523	
		(2, +2)	25 – 9	3.9040 – 5.0272	45 – 15	2.7425 – 3.5717	74 – 31	2.0663 – 2.5213	
	9	0	(1)	–	–	–	–	–	–
			(2)	–	–	–	–	35 – 19	0.4460 – 0.7921
100		(1, -1)	–	–	–	–	39 – 18	0.1934 – 0.3899	
		(1, +0)	–	–	–	–	29 – 20	0.3794 – 0.4833	
		(1, +1)	–	–	–	–	–	–	
		(2, -2)	–	–	16 – 11	0.1729 – 0.4235	42 – 18	(0.0421) – 0.3556	
		(2, -1)	–	–	17 – 11	0.5485 – 0.8059	45 – 18	0.2775 – 0.6381	
		(2, +0)	–	–	15 – 11	0.9182 – 1.1168	41 – 18	0.5092 – 0.8710	
200		(2, +1)	–	–	–	–	37 – 18	0.7352 – 1.0847	
		(2, +2)	–	–	–	–	33 – 18	0.9672 – 1.2884	
		(1, -1)	–	–	22 – 11	0.2191 – 0.4948	54 – 19	0.0508 – 0.3731	
		(1, +0)	–	–	–	–	41 – 19	0.4171 – 0.6173	
		(1, +1)	–	–	–	–	–	–	
		(2, -2)	–	–	23 – 11	(0.4953) – (0.0688)	54 – 19	(0.4811) – (0.0397)	
		(2, -1)	–	–	27 – 10	0.3795 – 0.8596	61 – 19	0.1776 – 0.6018	
		(2, +0)	–	–	23 – 11	0.9679 – 1.3527	54 – 19	0.6109 – 1.0132	
(2, +1)	–	–	18 – 11	1.5665 – 1.8618	46 – 19	1.0212 – 1.3907			
(2, +2)	–	–	–	–	35 – 19	1.4595 – 1.7554			

Table 3. The same as in Tab. 1 but for r modes and $V_{\text{rot}} = 100, 200 \text{ km s}^{-1}$.

Grid	$V_{\text{rot}} [\text{km s}^{-1}]$	mode (r, m)	$M [M_\odot]$	$\log T_{\text{eff}}$	$\log L/L_\odot$	$\log g$	$\nu [\text{d}^{-1}]$	$\Omega/\Omega_{\text{crit}}$
OP $X_0 = 0.70$ $Z = 0.015$	100	$(r, -1)$	2.65 – 7.80	4.025 – 4.268	1.71 – 3.67	3.67 – 4.34	0.0258 – 0.2217	0.30 – 0.46
		$(r, -2)$	2.50 – 6.80	4.010 – 4.235	1.61 – 3.46	3.69 – 4.34	0.4390 – 1.5478	0.30 – 0.46
		$(r, -3)$	2.45 – 6.20	3.999 – 4.210	1.58 – 3.31	3.70 – 4.34	0.8538 – 2.8766	0.31 – 0.46
		$(r, -4)$	2.40 – 5.70	3.990 – 4.189	1.54 – 3.18	3.70 – 4.34	1.2868 – 4.1687	0.32 – 0.47
	200	$(r, -1)$	2.85 – 11.00	4.046 – 4.333	1.82 – 4.17	3.56 – 4.28	0.0990 – 0.7868	0.56 – 0.86
		$(r, -2)$	2.75 – 9.40	4.033 – 4.301	1.76 – 3.94	3.59 – 4.28	0.7133 – 3.0166	0.57 – 0.87
		$(r, -3)$	2.65 – 8.40	4.023 – 4.277	1.70 – 3.77	3.60 – 4.28	1.3785 – 5.4245	0.58 – 0.87
		$(r, -4)$	2.60 – 7.70	4.014 – 4.258	1.67 – 3.64	3.62 – 4.28	2.0822 – 7.7980	0.58 – 0.88

of $V_{\text{rot}} = 100 \text{ km s}^{-1}$ and the $(r, -1)$ modes, the instability begins at a mass $M = 2.65 M_\odot$, the effective temperature $\log T_{\text{eff}} = 4.0248$, and extends over $5.15 M_\odot$ in mass and about 7900 K in effective temperature, whereas in the case of $(r, -4)$ the instability begins at a mass $M = 2.40 M_\odot$, the

effective temperature $\log T_{\text{eff}} = 3.9915$, and extends only over $3.40 M_\odot$ in mass and about 5800 K in effective temperature. We would like to emphasise that the lower boundary of the $(r, -4)$ modes is below 10 000 K. Perhaps this fact partly explains the presence of a significant number of pulsating

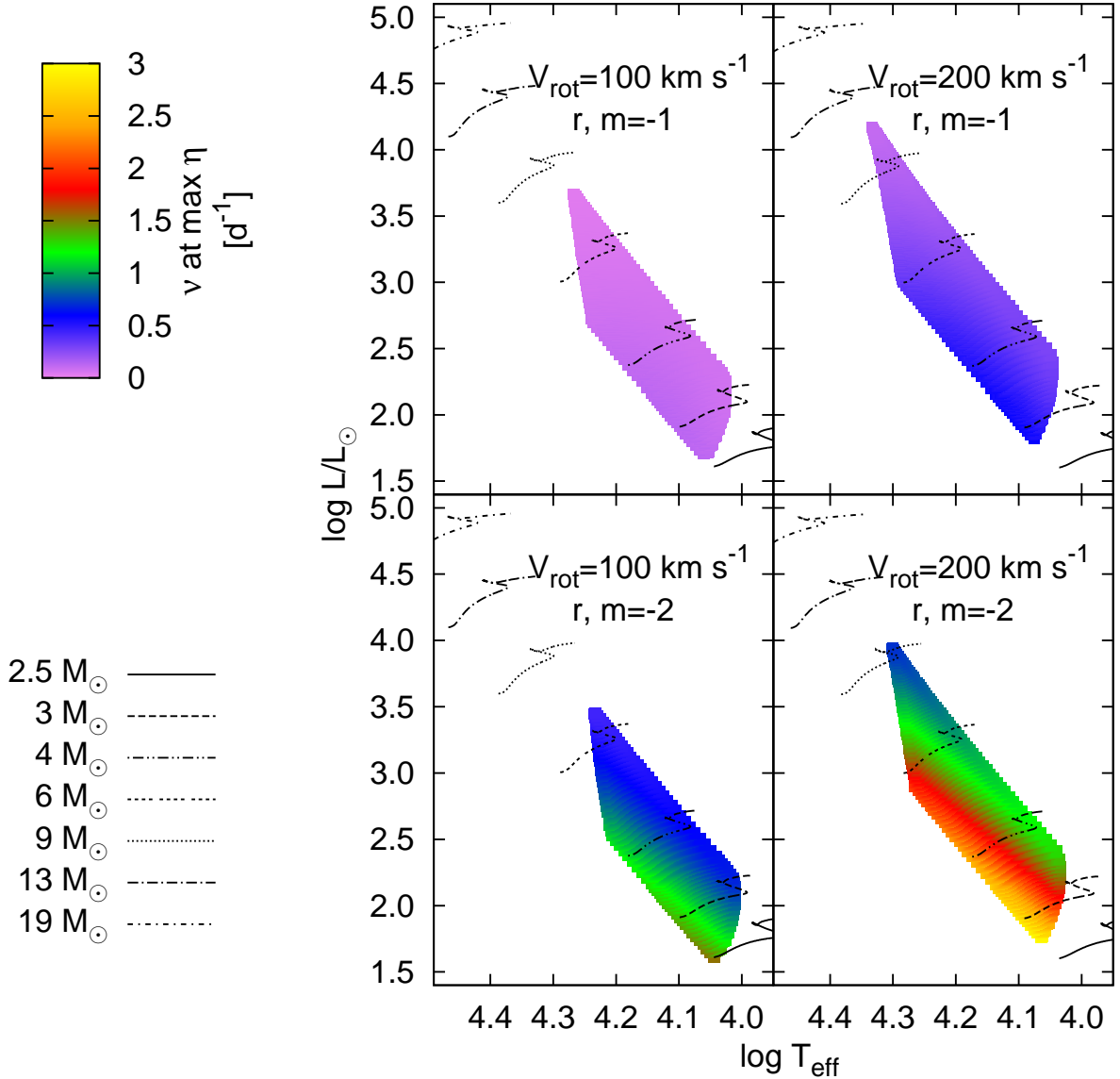


Figure 5. The same as in Fig. 2 but for the modes with r $m = -1, -2$ and $V_{\text{rot}} = 100$ and 200 km s^{-1} .

stars between the SPB and δ Sct instability strip found by Mowlavi et al. (2013) in the young open cluster NGC 3766. In this region, the instability strip of new-old class of variables (i.e., Maia stars, postulated already in the last century by Struve (1955)) may be located. The problem with the explanation of Maia stars in terms of r modes arises from their low visibility. But we do not know the intrinsic amplitudes of the modes. The majority of variable stars discovered by Mowlavi et al. (2013) appear to be fast rotators (Mowlavi et al. 2016). Salmon et al. (2014) tried to explain these stars in terms of prograde sectoral and r modes. They concluded that prograde sectoral modes in combination with the gravity darkening effect and fast rotation provide a satisfactory explanation of these stars.

We recall the fact that the r modes for a given model are unstable in a very narrow range of frequencies, which broadens with increasing value of V_{rot} and shrinks with increasing value of $|m|$ (e.g., Dziembowski et al. 2007). In addition, the range of frequencies of unstable modes in the whole instabil-

ity domain increases with increasing $|m|$ (see Table 3). This is due to the fact that for higher $|m|$ the frequencies of unstable modes vary more rapidly with the mass and effective temperature of the model than in the case of modes with lower $|m|$.

3 THE EFFECTS OF INPUT PARAMETERS ON THE EXTENT OF THE SPB INSTABILITY STRIP

The location and extent of the SPB instability strip on the H-R diagram are sensitive to different parameters of evolutionary models. Here, we examined the influence of the initial hydrogen abundance, X_0 , the metallicity, Z , overshooting from the convective core, α_{ov} , and the opacity data. Since only dipole modes are considered, figures from Appendix D should be compared with the reference models presented in Fig. 2.

Table 4. The same as in Table 1 but for other model grids, i. e., a grid with increased hydrogen abundance, $X_0 = 0.75$, a grid with decreased metallicity, $Z = 0.010$, a grid with overshooting from the convective core, $\alpha_{\text{ov}} = 0.2$ and a grid with the OPAL tables.

Grid	V_{rot} [km s^{-1}]	mode (ℓ, m)	M [M_{\odot}]	$\log T_{\text{eff}}$	$\log L/L_{\odot}$	$\log g$	ν [d^{-1}]	$\Omega/\Omega_{\text{crit}}$	
$X_0 = 0.75$ OP	$Z = 0.015$ $\alpha_{\text{ov}} = 0.0$	0	(1)	3.05 – 10.50	4.037 – 4.309	1.85 – 4.03	3.62 – 4.36	0.2008 – 1.5589	0.00
		100	(1, -1)	3.30 – 20.00*	4.070 – 4.411*	1.97 – 4.89*	3.41* – 4.34	0.0944 – 1.2553	0.27 – 0.44
			(1, +0)	3.15 – 12.10	4.051 – 4.335	1.90 – 4.23	3.57 – 4.34	0.2904 – 1.7049	0.28 – 0.45
		200	(1, +1)	2.95 – 9.40	4.025 – 4.284	1.79 – 3.86	3.62 – 4.34	0.4947 – 2.2073	0.29 – 0.45
			(1, -1)	3.60 – 20.00*	4.093 – 4.435*	2.11 – 4.89*	3.34* – 4.29	(0.0774) – 1.1671	0.52 – 0.83
			(1, +0)	3.35 – 20.00*	4.064 – 4.412*	1.99 – 4.89*	3.34* – 4.29	0.2758 – 1.9813	0.54 – 0.85
$X_0 = 0.70$ OP	$Z = 0.010$ $\alpha_{\text{ov}} = 0.0$	0	(1)	2.80 – 7.50	4.056 – 4.284	1.87 – 3.65	3.75 – 4.41	0.2849 – 1.6024	0.00
		100	(1, -1)	3.00 – 9.90	4.086 – 4.341	1.98 – 4.05	3.69 – 4.39	0.1566 – 1.3162	0.28 – 0.43
			(1, +0)	2.90 – 8.40	4.067 – 4.307	1.93 – 3.82	3.71 – 4.39	0.3818 – 1.8232	0.29 – 0.44
		200	(1, +1)	2.75 – 6.80	4.044 – 4.261	1.87 – 3.50	3.74 – 4.39	0.6368 – 2.3479	0.30 – 0.45
			(1, -1)	3.25 – 20.00*	4.108 – 4.441*	2.10 – 4.96*	3.43* – 4.34	(0.0375) – 1.2402	0.53 – 0.82
			(1, +0)	3.00 – 10.60	4.079 – 4.347	1.97 – 4.15	3.62 – 4.34	0.4527 – 2.1763	0.55 – 0.83
$X_0 = 0.70$ OP	$Z = 0.015$ $\alpha_{\text{ov}} = 0.2$	0	(1)	2.75 – 10.90	4.033 – 4.323	1.77 – 4.24	3.48 – 4.36	0.1746 – 1.6049	0.00
		100	(1)	18.50 – 20.00*	4.395 – 4.404*	4.92 – 5.01*	3.29* – 3.32	0.2129 – 0.2393	0.00
			(1, -1)	3.00 – 20.00*	4.067 – 4.428*	1.91 – 5.01*	3.25* – 4.34	0.0762 – 1.3118	0.28 – 0.47
		200	(1, +0)	2.85 – 20.00*	4.047 – 4.411*	1.83 – 5.01*	3.25* – 4.34	0.2096 – 1.7686	0.29 – 0.48
			(1, +1)	2.65 – 9.30	4.021 – 4.290	1.71 – 4.01	3.49 – 4.34	0.4271 – 2.3164	0.29 – 0.49
			(1, -1)	3.30 – 20.00*	4.091 – 4.451*	2.06 – 5.00*	3.10* – 4.28	(0.0923) – 1.2089	0.53 – 0.88
$X_0 = 0.70$ OPAL	$Z = 0.015$ $\alpha_{\text{ov}} = 0.0$	0	(1)	2.65 – 7.10	4.026 – 4.246	1.72 – 3.53	3.68 – 4.36	0.2291 – 1.6062	0.00
		100	(1, -1)	2.95 – 9.40	4.063 – 4.307	1.90 – 3.95	3.63 – 4.33	0.1066 – 1.2949	0.29 – 0.45
			(1, +0)	2.75 – 8.00	4.042 – 4.270	1.78 – 3.71	3.65 – 4.34	0.3310 – 1.7702	0.30 – 0.46
		200	(1, +1)	2.55 – 6.60	4.013 – 4.223	1.65 – 3.42	3.67 – 4.34	0.5799 – 2.3098	0.31 – 0.47
			(1, -1)	3.20 – 20.00*	4.087 – 4.422*	2.02 – 4.95*	3.33* – 4.28	(0.0866) – 1.1975	0.56 – 0.84
			(1, +0)	2.95 – 10.10	4.057 – 4.314	1.89 – 4.05	3.56 – 4.28	0.4007 – 2.0681	0.57 – 0.86
200	(1, +1)	2.55 – 6.80	4.009 – 4.224	1.65 – 3.46	3.60 – 4.28	0.8585 – 3.1699	0.60 – 0.89		

Increasing the initial hydrogen abundance from $X_0 = 0.70$ to $X_0 = 0.75$ (Fig. 2 vs. Fig. D1) shifts the instability strip to higher effective temperatures and masses. In the non-rotating case, unstable g modes appear at a mass higher by $0.3 M_{\odot}$ and disappear at a mass higher by $1.4 M_{\odot}$ compared to the reference models. The corresponding boundaries in effective temperature are shifted only by about 125 and 185 K, respectively.

If we consider lower boundaries of mass and effective temperature at the rotation velocity, $V_{\text{rot}} = 200 \text{ km s}^{-1}$, the g modes become unstable from a mass higher by $0.3 M_{\odot}$ and effective temperature higher by 115 K for retrograde modes, $0.35 M_{\odot}$ and 130 K for axisymmetric modes and $0.3 M_{\odot}$ and 120 K for prograde modes, compared to the reference models. Upper boundaries of mass and effective temperature, within the parameter space of our model grid, exist only for prograde modes. The boundary parameters for the instability domains are summarised in Table 4. As one can see, the shifts are rather small compared to those induced by the effects of rotation. A good example is the case of the (1, -1) modes at $V_{\text{rot}} = 200 \text{ km s}^{-1}$. In this case the low mass and effective temperature boundary is shifted by $0.55 M_{\odot}$ and 1500 K relative to the non-rotating models.

It should be noted that the difference between our reference models and those with increased hydrogen abundance is

associated with the change in the amount of the nuclear fuel and with the change of the free-free opacities in the central layers of the star. This results in shifting the evolutionary tracks on the H-R diagram; for a given effective temperature and luminosity, an increase of the hydrogen abundance reduces the mass of the corresponding model. However, this has a little impact on pulsation driving by the κ -mechanism.

The effect of decreasing the metallicity on the instability domain of dipole modes is shown in Fig. D2 where results for $Z = 0.010$ are depicted. Since the g-modes are excited by the κ -mechanism acting on the Z opacity bump, it is not a surprise that lower metallicity reduces the size of the instability strip. In the non-rotating case the g modes become unstable for masses higher by $0.05 M_{\odot}$ and effective temperature higher by 610 K and are stabilized for masses lower by $1.6 M_{\odot}$ and effective temperature lower by 955 K compared to our reference grid. When a star rotates with $V_{\text{rot}} = 200 \text{ km s}^{-1}$, the low effective temperature boundaries of the instability strip for all dipole modes are shifted to values higher by about 550 K relative to our reference grid.

Moreover, the instability extension to high masses observed for $Z = 0.015$ for axisymmetric modes disappears. In the case of retrograde modes, the instability appears in the whole range masses above $M = 3.25 M_{\odot}$. Similarly, only the lower boundary of effective temperature, $\log T_{\text{eff}} = 4.108$, can

be defined for the parameters of our grid of models (see also Table 4). Finally, in the case of prograde modes, the high mass and effective temperature instability border is shifted to lower values by $1.5 M_{\odot}$ and 905 K, respectively.

The effect of overshooting from the convective core is shown in Fig. D3. We applied the overshooting law proposed by Dziembowski & Pamyatnykh (2008), which is more smooth than usual step overshooting. The calculations were performed with overshooting parameter, $\alpha_{ov} = 0.2$. The convective core overshooting considerably prolongs the main sequence evolution causing wider instability domains. It means that for a given effective temperature, the instability strip reaches higher luminosities compared to the one found for the reference models. Moreover, overshooting expands the pulsational instability to higher luminosities, effective temperatures and masses. In the non-rotating models with $\alpha_{ov} = 0.2$, unstable dipole modes disappear at $10.9 M_{\odot}$ and appear again at about $18.5 M_{\odot}$ in contrast to our reference grid. As one can conclude from Fig. D3, the lower limit of the instability in the effective temperature is almost unchanged.

The instability domains for the dipole g modes obtained with the OPAL opacity tables are shown in Fig. D4 (see also Table 4). In comparison with our reference models they are smaller. The upper and lower boundaries of masses and effective temperatures are shifted towards smaller values. This is a well-known fact resulting from the deeper location of the Z-bump in the OP data compared to the OPAL data (e.g., Pamyatnykh 1999).

For the zero-rotation models, the instability is shifted at the low mass border by $0.1 M_{\odot}$ and 150 K and at the high mass border by $2 M_{\odot}$ and 2565 K.

In the models with $V_{rot} = 200 \text{ km s}^{-1}$, we found an extension of the instability strip to higher masses for retrograde modes but not for axisymmetric modes. In comparison with our reference grid, the low temperature instability boundary is shifted towards lower values by $0.1 M_{\odot}$ and 55 K for retrograde modes, by $0.05 M_{\odot}$ and 55 K for axisymmetric modes and by $0.1 M_{\odot}$ and 120 K for prograde modes.

Let us now discuss effects of different parameters on the values of unstable mode frequencies. For the purpose of clarity and brevity we focus only on dipole modes in non-rotating models. Let us recall that the dipole unstable modes in our reference models have frequencies in the range $\nu = 0.2162 - 1.6026 \text{ d}^{-1}$. Decreasing metallicity from $Z = 0.015$ to $Z = 0.010$ shifts the minimum frequency to slightly higher values by 0.07 d^{-1} , whereas the maximum frequency remains almost unchanged. A higher initial hydrogen abundance, $X_0 = 0.75$, shifts the minimum and maximum frequencies towards lower values, by 0.02 and 0.04 d^{-1} , respectively. Assuming $\alpha_{ov} = 0.2$ lowers the minimum frequency (by 0.04 d^{-1}) but does not change the highest frequency. Finally, using the OPAL tables results in increasing the minimum frequency by 0.01 d^{-1} whereas the value of the maximum frequency remains almost unchanged. As one can see, all these effects are noticeable but far smaller than the effects of rotation.

4 INSTABILITY DOMAINS OF THE DIPOLE MODES FOR FIXED VALUE OF Ω/Ω_{crit}

In order to compare our results with those of Townsend (2005a) and to show how non-constant Ω/Ω_{crit} affects instability strips, we computed a grid of models with the values of Ω/Ω_{crit} fixed at 0, 0.25 and 0.50. The remaining parameters were the same as for the reference models (see Section 2.1). The computations were limited to the dipole modes. The results are shown in Fig. 6 and are summarised in Table 5.

As one can see, the instability strips are slightly smaller than those computed for the fixed values of the equatorial velocity. This is due to the fact that the values of V_{rot} corresponding to the Ω/Ω_{crit} values used in this section are smaller than those used in preceding sections (see the last column of Table 5). Thus, the impact of rotation is smaller.

Our instability strips are much larger than those obtained by Townsend (2005a). In particular, we got much larger extension towards higher masses and higher effective temperatures on the H-R diagram. This is mainly due to the difference in the opacity data; Townsend (2005a) used the OPAL tables while we, the OP data. It has been already shown by Pamyatnykh (1999) for non-rotating models that such an extension of the instability strip exists if the OP opacities are used. Some differences can result also from adopting various chemical mixtures: GN93 in Townsend's computations vs. AGSS09 in ours.

Besides, we computed and compared instability strips for the non-rotating and rotating evolutionary models. It turns out that even such simple incorporation of rotation in the equilibrium models as we have done (see Section 2.1) affects the instability strips. Comparing the Townsend's and our instability strips, the reader has to bear in mind these differences.

5 INFLUENCE OF ROTATION ON PERIOD SPACING OF HIGH RADIAL-ORDER G MODES

For the present paper, the period spacing of high-order g modes is a side issue but recent discoveries of regular period patterns in B-type stars from space data (Degroote et al. 2010; Pápics et al. 2012, 2014, 2015) make it highly important. Moreover, the period spacing of g modes has been never discussed for massive stars such as β Cephei variables ($M = 8 - 16 M_{\odot}$). Here, we would like to emphasize that one should be careful while interpreting dense oscillation spectra obtained from space photometry. A good example is HD 50230: Degroote et al. (2010, 2012) claimed that they found regular period spacing in the CoRoT data, which is a manifestation of asymptotic behaviour, but our studies (Szewczuk et al. 2014) suggested rather that this regularity is spurious, i.e., the oscillation spectrum is composed of modes with various (ℓ, m) , and can not be interpreted according to the asymptotic theory.

For high radial-order g modes asymptotic theory predicts that period spacing, ΔP , defined as difference between periods of modes with the same spherical harmonic degree, ℓ , and consecutive radial orders, n , is constant (Tassoul 1980),

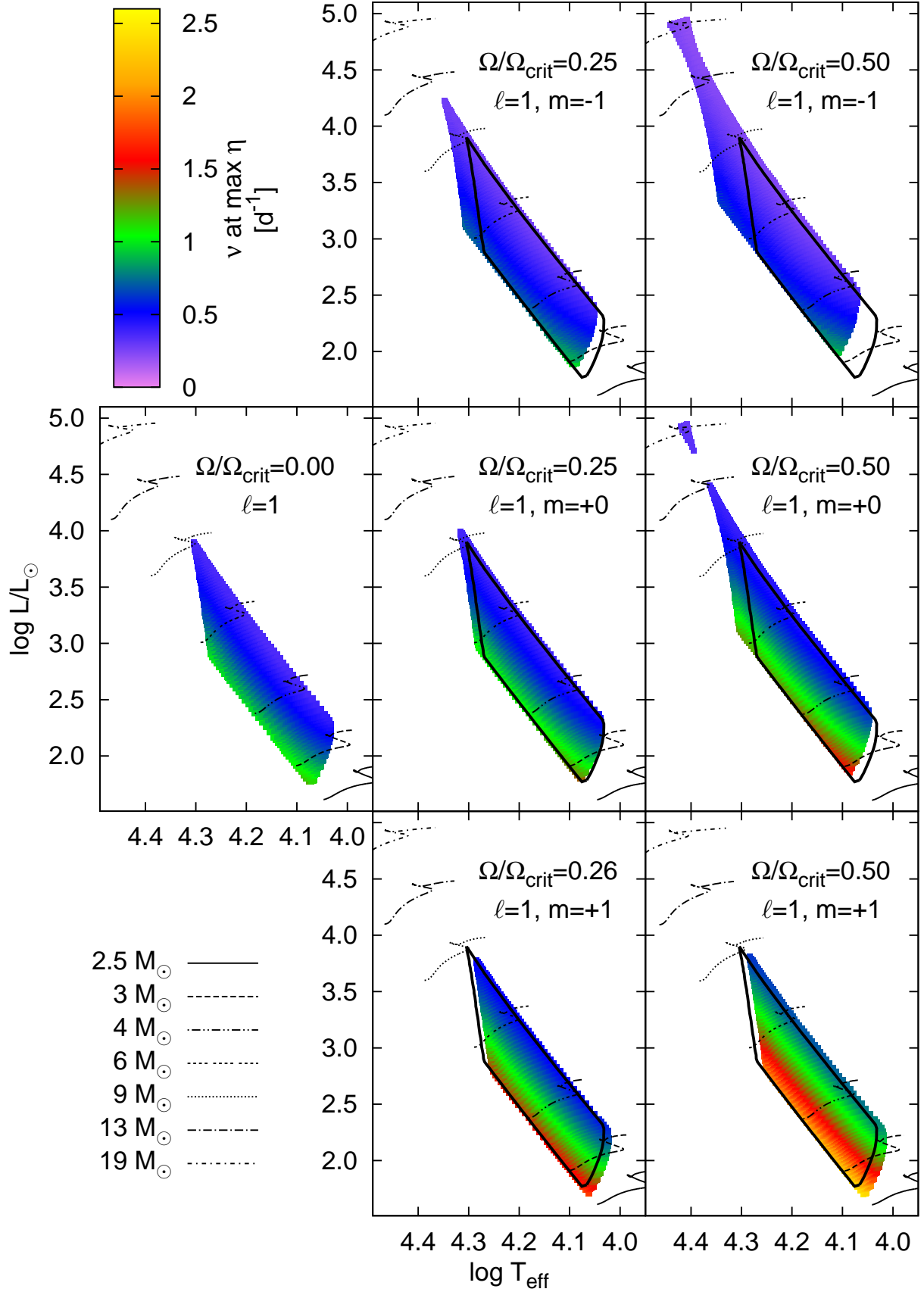


Figure 6. The same as in Fig. 2 but for the fixed ratio of the angular rotation velocity to its critical value, $\Omega/\Omega_{\text{crit}} = 0, 0.25$ and 0.5 .

Table 5. The same as in Tab. 1 but for fixed ratios of angular rotation rates to their critical values, $\Omega/\Omega_{\text{crit}} = 0.00, 0.25, 0.50$, and for dipole modes. In the last column there are given the ranges of the equatorial velocity.

Grid	$\Omega/\Omega_{\text{crit}}$	mode (ℓ, m)	M [M_{\odot}]	$\log T_{\text{eff}}$	$\log L/L_{\odot}$	$\log g$	ν [d^{-1}]	V_{rot} [km s^{-1}]	
OP	$X_0 = 0.70$	0.00	(1)	2.75 – 9.10	4.032 – 4.305	1.77 – 3.90	3.67 – 4.36	0.2162 – 1.6026	0
			(1, –1)	2.95 – 11.40	4.051 – 4.348	1.89 – 4.22	3.61 – 4.35	0.1454 – 1.3268	55 – 88
		0.25	(1, +0)	2.80 – 9.70	4.038 – 4.317	1.80 – 3.99	3.64 – 4.35	0.2678 – 1.7010	54 – 86
			(1, +1)	2.65 – 8.40	4.023 – 4.285	1.71 – 3.78	3.66 – 4.35	0.4124 – 2.1157	54 – 84
		0.50	(1, –1)	3.15 – 20.00*	4.069 – 4.441*	1.99 – 4.94*	3.31* – 4.32	0.0623 – 1.2546	112 – 183
			(1, +0)	2.90 – 13.00	4.047 – 4.362	1.85 – 4.40	3.51 – 4.32	0.3279 – 1.9390	110 – 177
	(1, +0)		16.50 – 20.00*	4.394 – 4.420*	4.71 – 4.94*	3.31* – 3.42	0.2641 – 0.3406	142 – 148	
	(1, +1)		2.65 – 8.60	4.018 – 4.284	1.70 – 3.81	3.61 – 4.32	0.6023 – 2.7352	108 – 169	

$$\Delta P_{\ell} = P_{n+1} - P_n = \frac{2\pi^2}{\sqrt{\ell(\ell+1)} \int_{r_1}^{r_2} N \, d \ln r} = \text{const}, \quad (1)$$

where r_1 and r_2 are the inner and outer turning points of the mode propagation cavity and N is the Brunt-Väisälä frequency which depends only on the equilibrium model. However, this result was obtained under zero-rotation and uniform chemical composition assumptions. When rotation is taken into account, the eigenvalue $\ell(\ell+1)$ has to be replaced by λ and ΔP in the co-rotating frame is given by (e. g., [Bouabid et al. 2013](#))

$$\Delta P_{\ell, m} = \frac{2\pi^2}{\sqrt{\lambda_{\ell, m, s(n+1)}} \int_{r_1}^{r_2} N \, d \ln r \left(1 + \frac{1}{2} \frac{d \ln \lambda_{\ell, m, s(n)}}{d \ln s} \right)}, \quad (2)$$

where subscripts in λ were added to emphasize the dependence on the angular indices and the spin parameter, which is itself a function of rotation and mode frequency. Therefore, in the case of rotating models ΔP , is no longer constant. Naturally, rotation changes also the equilibrium model and hence N .

An appropriate determination of ΔP is important because it is used in mode identification as well as an indicator of chemical abundance gradient on the boundary of the convective core, e. g., in the case of white dwarfs ([Winget et al. 1991](#)) and recently in SPB stars ([Degroote et al. 2010](#); [Pápics et al. 2014, 2015](#)). The behaviour of ΔP for the SPB-like models was studied also by [Dziembowski et al. \(1993\)](#) for non-rotating models and by [Aerts & Dupret \(2012\)](#) for rotating models but with rather low rotation velocity. Moreover, [Miglio et al. \(2008\)](#) derived an analytical approximation for the high-order g-mode periods that takes into account the effect of the chemical composition gradient near the core, ignoring all effects of rotation. For the zero-rotation case, their results are compatible with ours but since the authors used different masses we cannot make an adequate comparison.

In the present paper, we study the effects of rotation on the values of ΔP in the framework of the traditional approximation. In Fig. 7, we show ΔP as a function of period for dipole modes in the model with $M = 5 M_{\odot}$ and $\log T_{\text{eff}} = 4.180$. The calculations were performed for three values of the equatorial rotation: $V_{\text{rot}} = 1, 100$ and 200 km s^{-1} . We considered also three values of core overshooting: $\alpha_{\text{ov}} = 0.0, 0.2$ and 0.4 . As can be seen from Fig. 7, the

highest value of ΔP is obtained for retrograde sectoral modes ($m = -\ell$) and the lowest for prograde sectoral modes ($m = \ell$).

With increasing rotation, the deviation from the constant value of ΔP becomes more pronounced. An impact of convective core overshooting is rather minor and it is quantitatively comparable to the effect of slow rotation of the order of 1 km s^{-1} . Moreover, for intermediate radial orders one can clearly see the oscillatory behaviour of ΔP , a result already predicted by [Dziembowski et al. \(1993\)](#). The amplitude of this oscillation depends on the evolutionary stage, and more precisely, on the chemical composition gradient above the convective core. Furthermore, the amplitude of these oscillations decreases if core overshooting (as described by [Dziembowski & Pamyatnykh \(2008\)](#)) is included, this is a natural consequence of adding any partial mixing which blurs the chemical composition gradients.

In general, ΔP is a function of many variables; the most important are (ℓ, m), V_{rot} , M , T_{eff} , Z , X_0 , evolutionary stage or core overshooting. However, except for very slow rotation, the impact of V_{rot} overwhelms the effects of other parameters.

In a similar way as for the $5 M_{\odot}$ model, we tested the effect of rotation and core overshooting on ΔP in the more massive model with $M = 10 M_{\odot}$ and $\log T_{\text{eff}} = 4.360$ (see Fig. 8). As one can see from the figure, the qualitative properties are quite similar to those seen in Fig. 7 but the values of the mean period spacing are higher for higher-mass models.

The period spacings were modeled for, eg., KIC 10526294 ([Moravveji et al. 2015](#)) or KIC 7760680 ([Moravveji et al. 2016](#)) without and with the effects of rotation taken into account, respectively. The main problem in these studies was related to the instability conditions for some observed frequencies. As has been shown recently by [Szewczuk et al. \(2017\)](#), this problem can be solved by an appropriate enhancement of the opacities. In [Szewczuk et al. \(2017\)](#), we successfully reproduced both the value of the period spacing and the frequency range of unstable modes in the rotating SPB star KIC 7760680. Earlier, [Savonije \(2013\)](#) did not succeed in reproducing the period spacing in HD 43317. Let us repeat that it is easy to confuse period spacing resulting from asymptotic behaviour with accidental distribution of frequencies in dense oscillation spectrum (see [Szewczuk et al. 2014](#)).

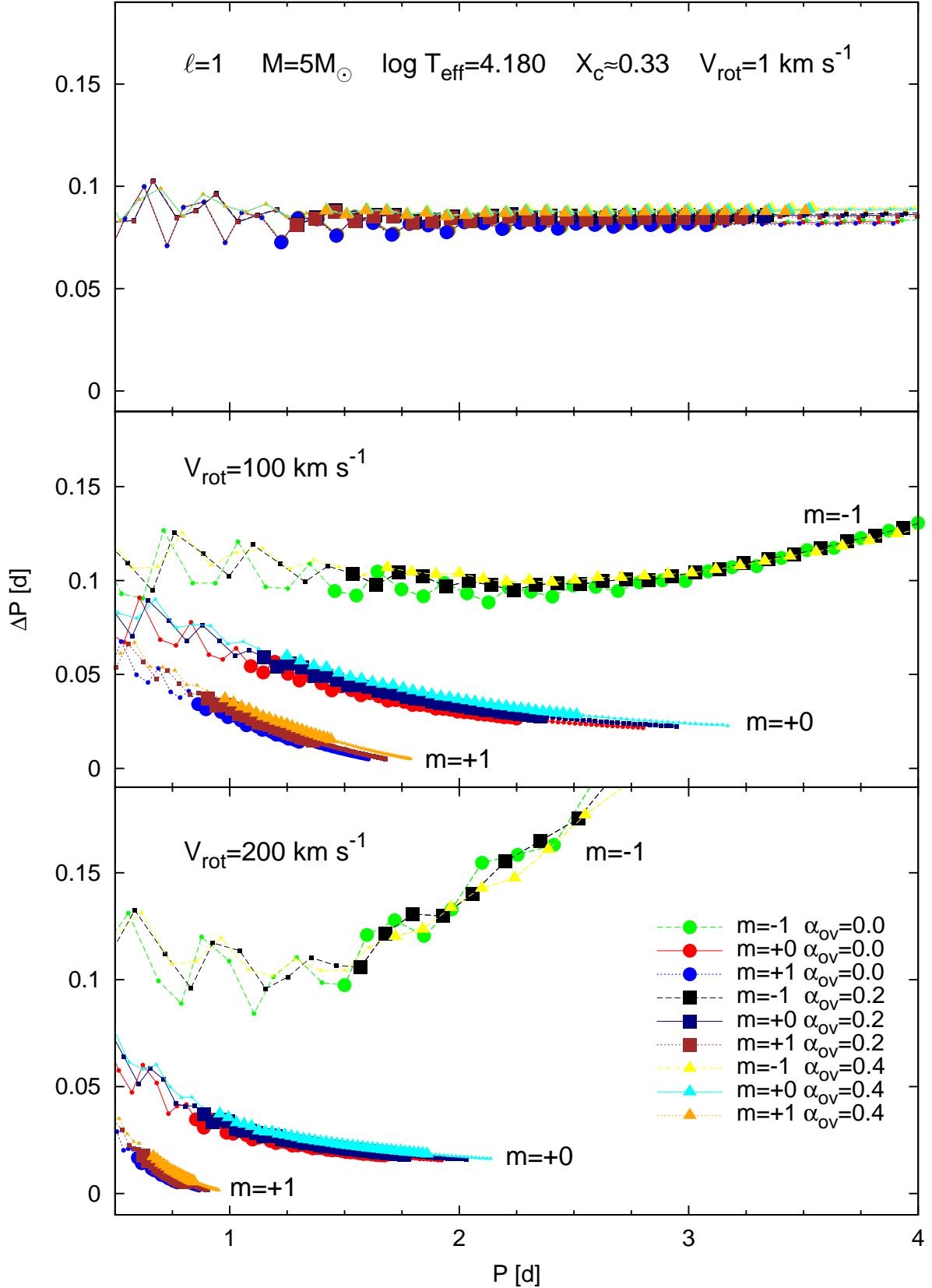


Figure 7. The period spacing for the dipole modes with $m = -1, 0$ and $+1$ in stellar model with $M = 5M_{\odot}$, $\log T_{\text{eff}} = 4.180$, $Z = 0.017$, $X_c \approx 0.33$, computed with the OP opacities and the AGSS09 chemical mixture. The three values of the rotation velocity, $V_{\text{rot}} = 1, 100, 200 \text{ km s}^{-1}$, and three values of the core overshooting parameter, $\alpha_{\text{ov}} = 0.0, 0.2, 0.4$, were examined. Pulsationally unstable modes are marked by larger symbols.

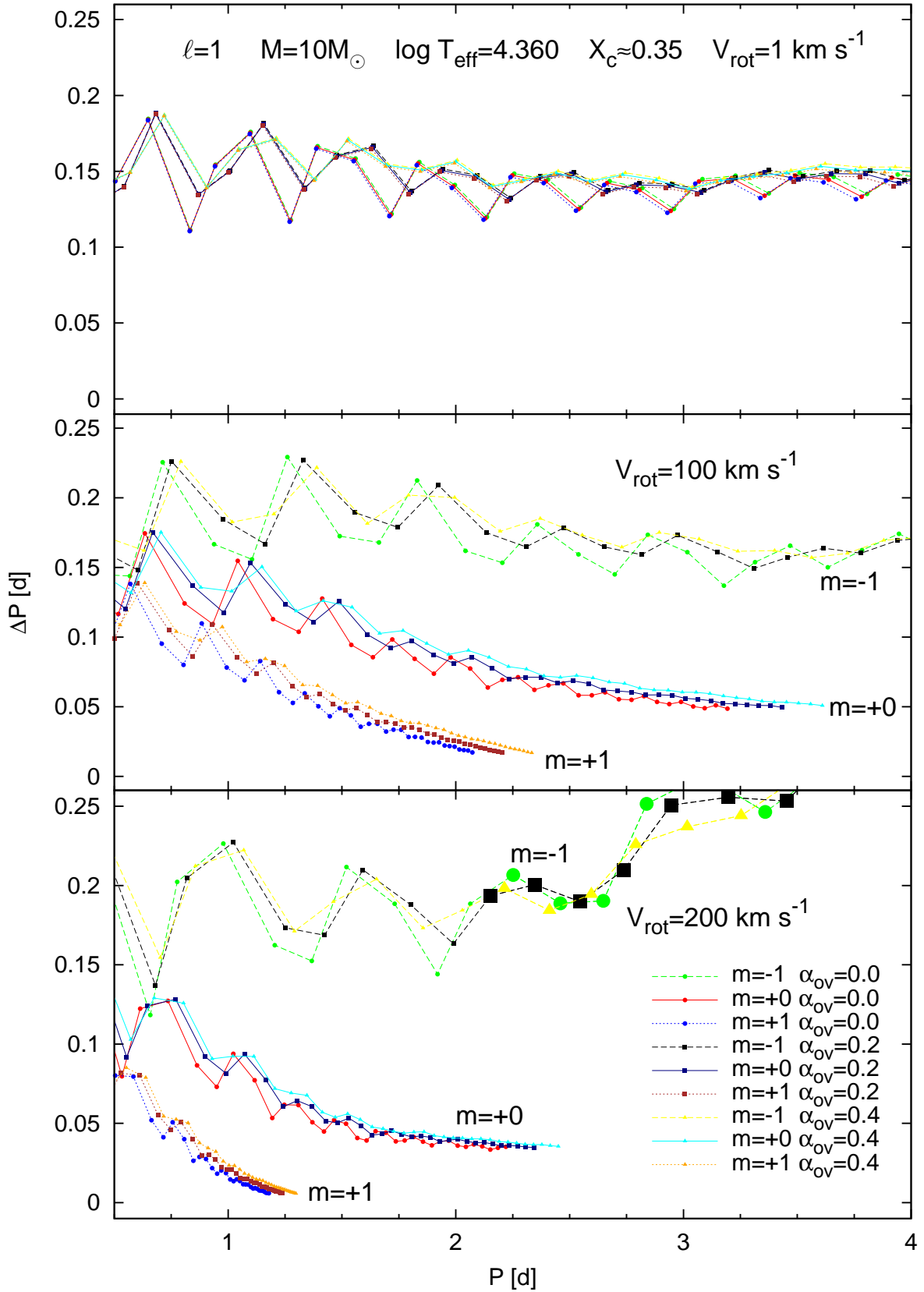


Figure 8. The same as in Fig. 7 but for $10M_{\odot}$ model with $\log T_{\text{eff}} = 4.360$ and $X_c \approx 0.35$.

6 SUMMARY

We presented results of extensive computations of gravity and mixed gravity–Rossby modes instability domains for stellar models with masses 2–20 M_{\odot} . The effects of rotation on pulsations were included using the traditional approximation which can be safely applied for slow–to–moderate rotators. We considered high–order g modes with ℓ up to 4 and mixed gravity–Rossby modes with $|m|$ up to 4. The latter modes become propagative only in the presence of rotation.

We relied on the equilibrium models computed with the Warsaw–New Jersey code which takes into account the mean effects of the centrifugal force whereas all effects of rotationally-induced mixing are ignored. Our results give a good qualitative picture of pulsational instability of slow modes in rotating B–type main sequence models. For a more detailed seismic analysis of individual objects, a more advanced evolutionary code, e.g., MESA, should be used.

We limited our computations to the rotation rate $\Omega \lesssim 0.7\Omega_{\text{crit}}$. This value was exceeded for a small number of evolved models with lowest masses. In these cases the frequencies and the instability parameter can be inaccurate.

In comparison with the results of Townsend (2005a), we obtained the g–mode instability domains on the H–R diagram much more extended towards higher masses and higher effective temperatures. This is mainly due to the difference in the opacity data (OPAL vs. OP). We found that in the case of rotating models, the extension occurs also for the OPAL opacity data (cf. Fig. D4 for $V_{\text{rot}} = 200 \text{ km s}^{-1}$). Thus, another reason for the difference between our and Townsend’s results is the higher rotation rate we used. Some differences may have arisen from adopting different chemical mixtures (GN93 vs. AGSS09). Finally, including mean effects of the centrifugal force in our equilibrium models also had a not negligible effect.

We would like to emphasize that in the rotating models, the unstable prograde high radial–order g modes may have quite high frequencies, typically not associated with SPB–like pulsation. This fact is especially important in the era of high precision space photometry where modes with higher degree, $\ell \geq 3$, can be detected. The important result is also that for the rotating models, we obtained a wider instability strip for a given ℓ than in the non–rotating case. Moreover, the shift of the lower boundary of the effective temperature to the lower values for prograde sectoral modes ($\ell = m$), combined with their high frequencies caused by rotation, can possibly explain the existence of some Maia stars (e.g., Balona et al. 2015). Moreover, r modes can also, at least partially, fill the gap between the SPB and δ Sct instability domains, exactly where Mowlavi et al. (2013) found a new class of pulsating stars. The role of the fast rotation in the phenomenon of pulsating stars located between the SPB and δ Scuti instability strip was already discussed in the literature (e.g. Mowlavi et al. 2013; Salmon et al. 2014; Mowlavi et al. 2016; Daszynska-Daszkievicz et al. 2017; Saio et al. 2017).

Variable stars similar to those of Mowlavi et al. (2013) were also observed in NGC 457 (Moździerski et al. 2014) and NGC 884 (Saesen et al. 2010, 2013). Some of them exhibit much too high frequencies for the SPB stars or seem to lie below the classical SPB instability strip. Using parameters

given by Saesen et al. (2013), we plotted variables observed in NGC 884 on the H–R diagram and compared with our instability strips. It turned out that the location and the high frequencies of all but one Maia-like star can be explained by prograde sectoral modes excited in fast rotating models of SPB stars (see also Appendix E).

Recently, Szewczuk & Daszyńska-Daszkiewicz (2015) compiled the parameters of SPB stars. The observed parameters of the SPB stars in their list are consistent in terms of both the position on the H–R diagram and the excited frequencies with the calculations presented in the present paper.

There is also well known problem with the so called macroturbulence, i.e. the line–profile broadening cause by other factors than rotation (e.g. Simón-Díaz & Herrero 2014). Recently, Aerts et al. (2009) showed that macroturbulence could be a signature of collective effect of pulsations. However, Simón-Díaz et al. (2017); Godart et al. (2017) argued that alone heat driven pulsations can not explain the occurrence of macroturbulence. Not all stars with macroturbulent broadening fall into instability strips. In Section 2 we obtained wider instability strips than Simón-Díaz et al. (2017) and Godart et al. (2017). In particular, we showed that the instability of high–order g modes begins at earlier evolutionary stage for massive stars than found by Simón-Díaz et al. (2017) and Godart et al. (2017). These differences are caused mainly by the circumstance that they used an older chemical mixture (GN93) and ignored the effects of rotation. Taking into account modes with ℓ up to 20 as was done by Godart et al. (2017) could give us even more extend instability domains than those presented in the present paper. Unfortunately, we did not study instability condition beyond the main sequence where many stars with significant macroturbulent broadening are located. This task is planned for the near future.

Finally, we showed that the initial hydrogen abundance, metallicity, overshooting from the convective core and a source of the opacity data have a minor influence on the extent of the SPB instability domains in comparison with the effects of rotation.

ACKNOWLEDGEMENTS

We thank Mikołaj Jerzykiewicz for careful reading of the manuscript and language corrections. This work was financially supported by the Polish National Science Centre grant 2015/17/B/ST9/02082. Calculations have been carried out using resources provided by Wrocław Centre for Networking and Supercomputing (<http://wcss.pl>), grant no. 265.

REFERENCES

- Aerts C., Dupret M.-A., 2012, in Shibahashi H., Takata M., Lynas-Gray A. E., eds, *Astronomical Society of the Pacific Conference Series Vol. 462, Progress in Solar/Stellar Physics with Helio- and Asteroseismology*. p. 103 ([arXiv:1108.6248](https://arxiv.org/abs/1108.6248))
 Aerts C., Puls J., Godart M., Dupret M.-A., 2009, *A&A*, **508**, 409
 Aprilia Lee U., Saio H., 2011, *MNRAS*, **412**, 2265
 Asplund M., Grevesse N., Sauval A. J., 2005, in Barnes III T. G., Bash F. N., eds, *Astronomical Society of the Pacific Confer-*

- ence Series Vol. 336, Cosmic Abundances as Records of Stellar Evolution and Nucleosynthesis. p. 25
- Asplund M., Grevesse N., Sauval A. J., Scott P., 2009, *ARA&A*, **47**, 481
- Bahcall J. N., Pinsonneault M. H., Wasserburg G. J., 1995, *Reviews of Modern Physics*, **67**, 781
- Bailey J. E., et al., 2015, *Nature*, **517**, 56
- Ballot J., Lignières F., Prat V., Reese D. R., Rieutord M., 2012, in Shibahashi H., Takata M., Lynas-Gray A. E., eds, *Astronomical Society of the Pacific Conference Series Vol. 462, Progress in Solar/Stellar Physics with Helio- and Asteroseismology*. p. 389
- Ballot J., Lignières F., Reese D. R., 2013, in Goupil M., Belkacem K., Neiner C., Lignières F., Green J. J., eds, *Lecture Notes in Physics, Berlin Springer Verlag Vol. 865, Lecture Notes in Physics, Berlin Springer Verlag*. p. 91, doi:10.1007/978-3-642-33380-4_5
- Balona L. A., et al., 2011, *MNRAS*, **413**, 2403
- Balona L. A., Baran A. S., Daszyńska-Daszkiewicz J., De Cat P., 2015, *MNRAS*, **451**, 1445
- Bouabid M.-P., Dupret M.-A., Salmon S., Montalbán J., Miglio A., Noels A., 2013, *MNRAS*, **429**, 2500
- Castelli F., Kurucz R. L., 2003, in Piskunov N., Weiss W. W., Gray D. F., eds, *IAU Symposium Vol. 210, Modelling of Stellar Atmospheres*. p. A20
- Chapellier E., Le Contel D., Le Contel J. M., Mathias P., Valtier J.-C., 2006, *A&A*, **448**, 697
- Colgan J., et al., 2013, *High Energy Density Physics*, **9**, 369
- Colgan J., Kilcrease D. P., Magee N. H., Abdallah J., Sherrill M. E., Fontes C. J., Hakel P., Zhang H. L., 2015, *High Energy Density Physics*, **14**, 33
- Cox A. N., Morgan S. M., Rogers F. J., Iglesias C. A., 1992, *ApJ*, **393**, 272
- Cugier H., 2014, *A&A*, **565**, A76
- Daszynska-Daszkiewicz J., Dziembowski W. A., Pamyatnykh A. A., 2007, *Acta Astron.*, **57**, 11
- Daszyńska-Daszkiewicz J., Dziembowski W. A., Pamyatnykh A. A., 2008, *Journal of Physics Conference Series*, **118**, 012024
- Daszyńska-Daszkiewicz J., Dziembowski W. A., Jerzykiewicz M., Handler G., 2015, *MNRAS*, **446**, 1438
- Daszynska-Daszkiewicz J., Walczak P., Pamyatnykh A., 2017, preprint, ([arXiv:1701.00937](https://arxiv.org/abs/1701.00937))
- Degroote P., et al., 2010, *Nature*, **464**, 259
- Degroote P., et al., 2012, *A&A*, **542**, A88
- Dziembowski W. A., Pamyatnykh A. A., 2008, *MNRAS*, **385**, 2061
- Dziembowski W. A., Moskalik P., Pamyatnykh A. A., 1993, *MNRAS*, **265**, 588
- Dziembowski W. A., Daszyńska-Daszkiewicz J., Pamyatnykh A. A., 2007, *MNRAS*, **374**, 248
- Ferguson J. W., Alexander D. R., Allard F., Barman T., Bodnarik J. G., Hauschildt P. H., Heffner-Wong A., Tamanai A., 2005, *ApJ*, **623**, 585
- Frost E. B., 1902, *ApJ*, **15**
- Gautschy A., Saio H., 1993, *MNRAS*, **262**, 213
- Godart M., Simón-Díaz S., Herrero A., Dupret M. A., Grötsch-Noels A., Salmon S. J. A. J., Ventura P., 2017, *A&A*, **597**, A23
- Grevesse N., Noels A., 1993, in Prantzos N., Vangioni-Flam E., Casse M., eds, *Origin and Evolution of the Elements*. pp 15–25
- Handler G., et al., 2006, *MNRAS*, **365**, 327
- Huang W., Gies D. R., 2006, *ApJ*, **648**, 580
- Iglesias C. A., Rogers F. J., 1996, *ApJ*, **464**, 943
- Jerzykiewicz M., Handler G., Shobbrook R. R., Pigulski A., Medupe R., Mokgwetsi T., Tlhagwane P., Rodríguez E., 2005, *MNRAS*, **360**, 619
- Lee U., 2001, *ApJ*, **557**, 311
- Lee U., 2006, *MNRAS*, **365**, 677
- Lee U., 2008, *Communications in Asteroseismology*, **157**, 203
- Lee U., Saio H., 1989, *MNRAS*, **237**, 875
- Lee U., Saio H., 1997, *ApJ*, **491**, 839
- Marsh Boyer A. N., McSwain M. V., Aragona C., Ou-Yang B., 2012, *AJ*, **144**, 158
- McNamara B. J., Jackiewicz J., McKeever J., 2012, *AJ*, **143**, 101
- Miglio A., Montalbán J., Dupret M.-A., 2007a, *Communications in Asteroseismology*, **151**, 48
- Miglio A., Montalbán J., Dupret M.-A., 2007b, *MNRAS*, **375**, L21
- Miglio A., Montalbán J., Noels A., Eggenberger P., 2008, *MNRAS*, **386**, 1487
- Moravveji E., 2016, *MNRAS*, **455**, L67
- Moravveji E., Aerts C., Pápics P. I., Triana S. A., Vandoren B., 2015, *A&A*, **580**, A27
- Moravveji E., Townsend R. H. D., Aerts C., Mathis S., 2016, *ApJ*, **823**, 130
- Moskalik P., Dziembowski W. A., 1992, *A&A*, **256**, L5
- Mowlavi N., Barblan F., Saesen S., Eyer L., 2013, *A&A*, **554**, A108
- Mowlavi N., Saesen S., Semaan T., Eggenberger P., Barblan F., Eyer L., Ekström S., Georgy C., 2016, *A&A*, **595**, L1
- Moździerski D., Pigulski A., Kopacki G., Kołaczkowski Z., Stęślicki M., 2014, *Acta Astron.*, **64**, 89
- Pamyatnykh A. A., 1999, *Acta Astron.*, **49**, 119
- Pamyatnykh A. A., Dziembowski W. A., Handler G., Pikall H., 1998, *A&A*, **333**, 141
- Pápics P. I., et al., 2012, *A&A*, **542**, A55
- Pápics P. I., Moravveji E., Aerts C., Tkachenko A., Triana S. A., Bloemen S., Southworth J., 2014, *A&A*, **570**, A8
- Pápics P. I., Tkachenko A., Aerts C., Van Reeth T., De Smedt K., Hillen M., Østensen R., Moravveji E., 2015, *ApJ*, **803**, L25
- Pigulski A., et al., 2016, *A&A*, **588**, A55
- Rogers F. J., Nayfonov A., 2002, *ApJ*, **576**, 1064
- Saesen S., et al., 2010, *A&A*, **515**, A16
- Saesen S., Briquet M., Aerts C., Miglio A., Carrier F., 2013, *AJ*, **146**, 102
- Saio H., Ekström S., Mowlavi N., Georgy C., Saesen S., Eggenberger P., Semaan T., Salmon S. J. A. J., 2017, preprint, ([arXiv:1702.02306](https://arxiv.org/abs/1702.02306))
- Salmon S., Montalbán J., Morel T., Miglio A., Dupret M.-A., Noels A., 2012, *MNRAS*, **422**, 3460
- Salmon S. J. A. J., Montalbán J., Reese D. R., Dupret M.-A., Eggenberger P., 2014, *A&A*, **569**, A18
- Savonije G. J., 2005, *A&A*, **443**, 557
- Savonije G. J., 2013, *A&A*, **559**, A25
- Seaton M. J., 1996, *MNRAS*, **279**, 95
- Seaton M. J., 2005, *MNRAS*, **362**, L1
- Simón-Díaz S., Herrero A., 2014, *A&A*, **562**, A135
- Simón-Díaz S., Godart M., Castro N., Herrero A., Aerts C., Puls J., Telting J., Grassitelli L., 2017, *A&A*, **597**, A22
- Stankov A., Handler G., 2005, *ApJS*, **158**, 193
- Strom S. E., Wolff S. C., Dror D. H. A., 2005, *AJ*, **129**, 809
- Struve O., 1955, *Sky & Telesc.*, **14**
- Szewczuk W., Daszyńska-Daszkiewicz J., 2015, *MNRAS*, **450**, 1585
- Szewczuk W., Daszyńska-Daszkiewicz J., Dziembowski W., 2014, in Guzik J. A., Chaplin W. J., Handler G., Pigulski A., eds, *IAU Symposium Vol. 301, Precision Asteroseismology*. pp 109–112 ([arXiv:1311.2818](https://arxiv.org/abs/1311.2818)), doi:10.1017/S1743921313014178
- Szewczuk W., Daszyńska-Daszkiewicz J., Walczak P., 2017, preprint, ([arXiv:1701.01256](https://arxiv.org/abs/1701.01256))
- Tassoul M., 1980, *ApJS*, **43**, 469
- Townsend R. H. D., 2003a, *MNRAS*, **340**, 1020
- Townsend R. H. D., 2003b, *MNRAS*, **343**, 125
- Townsend R. H. D., 2005a, *MNRAS*, **360**, 465
- Townsend R. H. D., 2005b, *MNRAS*, **364**, 573
- Turck-Chièze S., et al., 2013, *High Energy Density Physics*, **9**, 473
- Waelkens C., 1991, *A&A*, **246**, 453

- Walczak P., Fontes C. J., Colgan J., Kilcrease D. P., Guzik J. A., 2015, *A&A*, 580, L9
- Walker G. A. H., et al., 2005, *ApJ*, 635, L77
- Winget D. E., et al., 1991, *ApJ*, 378, 326
- Zdravkov T., Pamyatnykh A. A., 2008, *Journal of Physics Conference Series*, 118, 012079

APPENDIX A: THE DISTRIBUTION OF $\Omega/\Omega_{\text{CRIT}}$ ACROSS THE CONSIDERED MASS RANGE

In Fig. A1, we depicted the distribution of the values of $\Omega/\Omega_{\text{crit}}$ corresponding to the rotation velocity, $V_{\text{rot}} = 100$ and 200 km s^{-1} . The reference models, as described in the text, were considered, i.e., the models with masses $2-20 M_{\odot}$ computed for $X_0 = 0.7$, $Z = 0.015$, OP data and the AGSS09 chemical mixture.

APPENDIX B: INSTABILITY DOMAINS FOR THE G MODES WITH $\ell = 3, 4$ AND MIXED GRAVITY-ROSSBY MODES WITH $M = -3, -4$

Here, we show the pulsation instability strips for the g modes with $\ell = 3$ and 4 (Fig B1–B6) and r modes with $m = -3$ and -4 (Fig B7) excited in the rotating reference models described in Section 2. Again the three values of the rotation velocity were considered, $V_{\text{rot}} = 0, 100, 200 \text{ km s}^{-1}$.

APPENDIX C: FREQUENCY EVOLUTION OF UNSTABLE G MODES IN SELECTED MODELS

Besides calculations of the instability strips, an interesting issue is the change of the pulsational frequencies and of the range of unstable mode frequencies with evolution. We present such results for the modes excited in our reference models with masses $M = 4, 6, 9 M_{\odot}$. As before, three values of the rotation velocity were chosen, $V_{\text{rot}} = 0, 100, 200 \text{ km s}^{-1}$. Figs. C1–C3 are for the dipole modes whereas Fig. C4 is for modes with $\ell = 2, 3, 4$ for a mass $M = 4 M_{\odot}$.

APPENDIX D: EFFECTS OF THE INPUT PARAMETERS ON THE EXTENT OF THE SPB INSTABILITY STRIP

Here, we show figures presenting effects of the input parameters on the extent of the instability strip of the dipole g-modes. There are shown the effects of the initial hydrogen abundance, X_0 , metallicity, Z , overshooting from the convective core, α_{ov} , and the opacity data. To see the influence of these parameters, all figures have to be compared with Fig. 2 of Section 2.1.

APPENDIX E: MAIA OR SPB STARS IN NGC 884

NGC 884 is a young open cluster, $\log(t/\text{yr}) = 7.12 - 7.28$, containing many SPB stars with unusually high frequencies (Saesen et al. 2010, 2013). For some of them, there are known

the values of the projected rotation velocity; they are all fast rotators with $V_{\text{rot}} \sin i$ well above 100 km s^{-1} in most cases (Strom et al. 2005; Huang & Gies 2006; Marsh Boyer et al. 2012).

We plotted all variables from the cluster on the H–R diagram (Fig. E1) and marked dominant frequency and the instability strips presented in the main paper. The stars, especially in the lower part of the diagram, are located near the ZAMS in accordance with the young age of the cluster. Moreover, as one can see from the figure, in the region where the SPB stars should be located there are many variables with frequencies in the range from about 2 to 6 d^{-1} . Non-rotating models cannot explain these frequencies, but unstable prograde sectoral dipole and quadrupole modes in rotating models can explain easily the range of the observed frequencies.

The only exception is the star Oo 2151. It falls close to the $r, m = -4$ mode instability domain but the frequency seems to be too high. However, the star’s luminosity greatly exceeds that of other stars with similar T_{eff} in the cluster. Moreover, the determination of the effective temperature of the star is uncertain because it lacks Geneva colour indices from which Saesen et al. (2013) have derived T_{eff} of most SPB variables of the cluster.

In the case of multiperiodic variables we also compared further frequencies with our models. On first sight, it seems that only two cases, $\nu_2 = 12.0 \text{ d}^{-1}$ in Oo 2323 and $\nu_3 = 12.6 \text{ d}^{-1}$ in Oo 2566 cannot be explained by our models. But then there is no certainty that they are of pulsational origin.

This paper has been typeset from a $\text{T}_{\text{E}}\text{X}/\text{L}^{\text{A}}\text{T}_{\text{E}}\text{X}$ file prepared by the author.

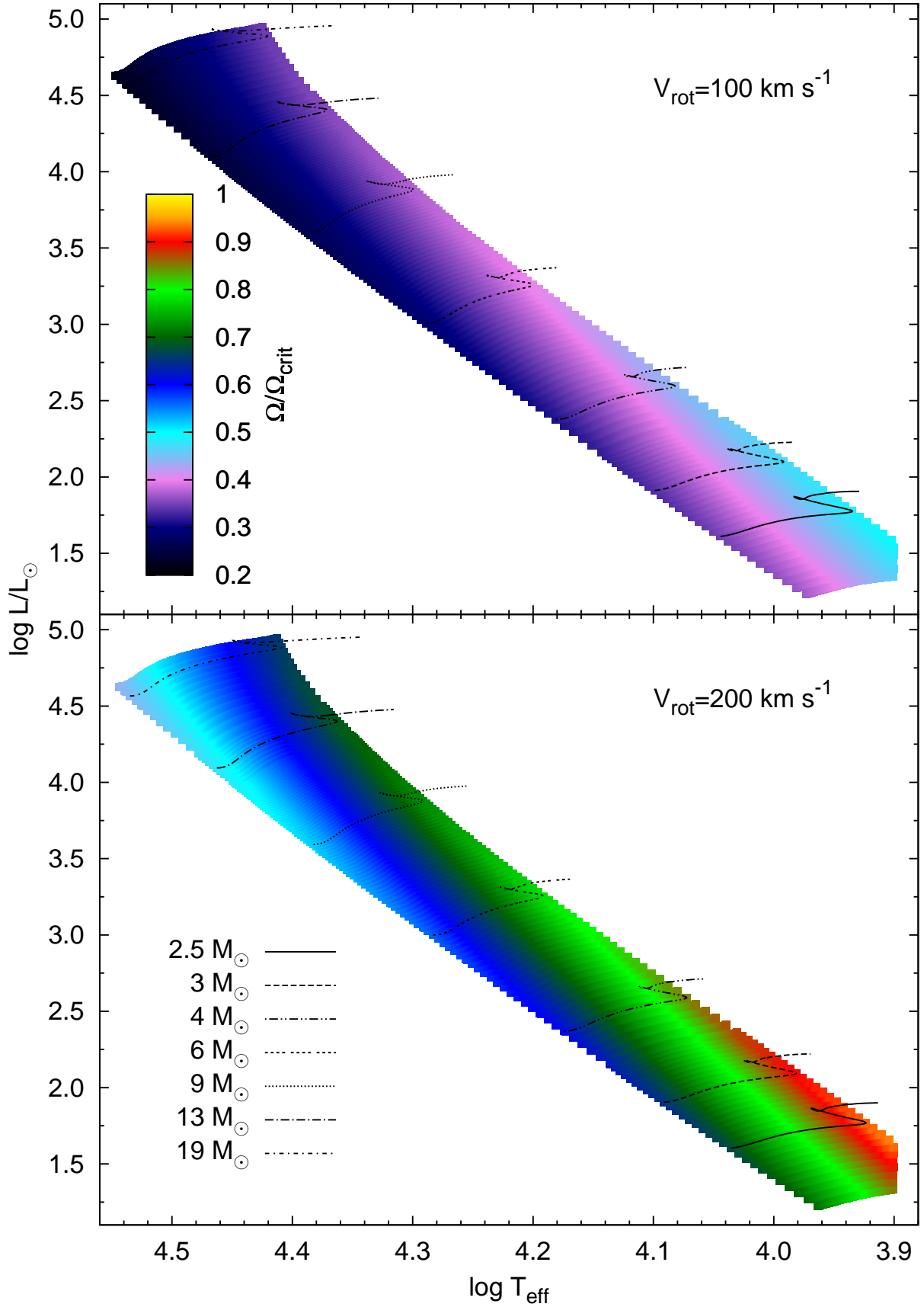


Figure A1. The distribution of the value of $\Omega/\Omega_{\text{crit}}$ corresponding to the rotation velocity, $V_{\text{rot}} = 100$ (the upper panel) and 200 km s^{-1} (the lower panel) across the H-R diagram. Models from our reference grid with the masses $M = 2 - 20 M_{\odot}$ are considered.

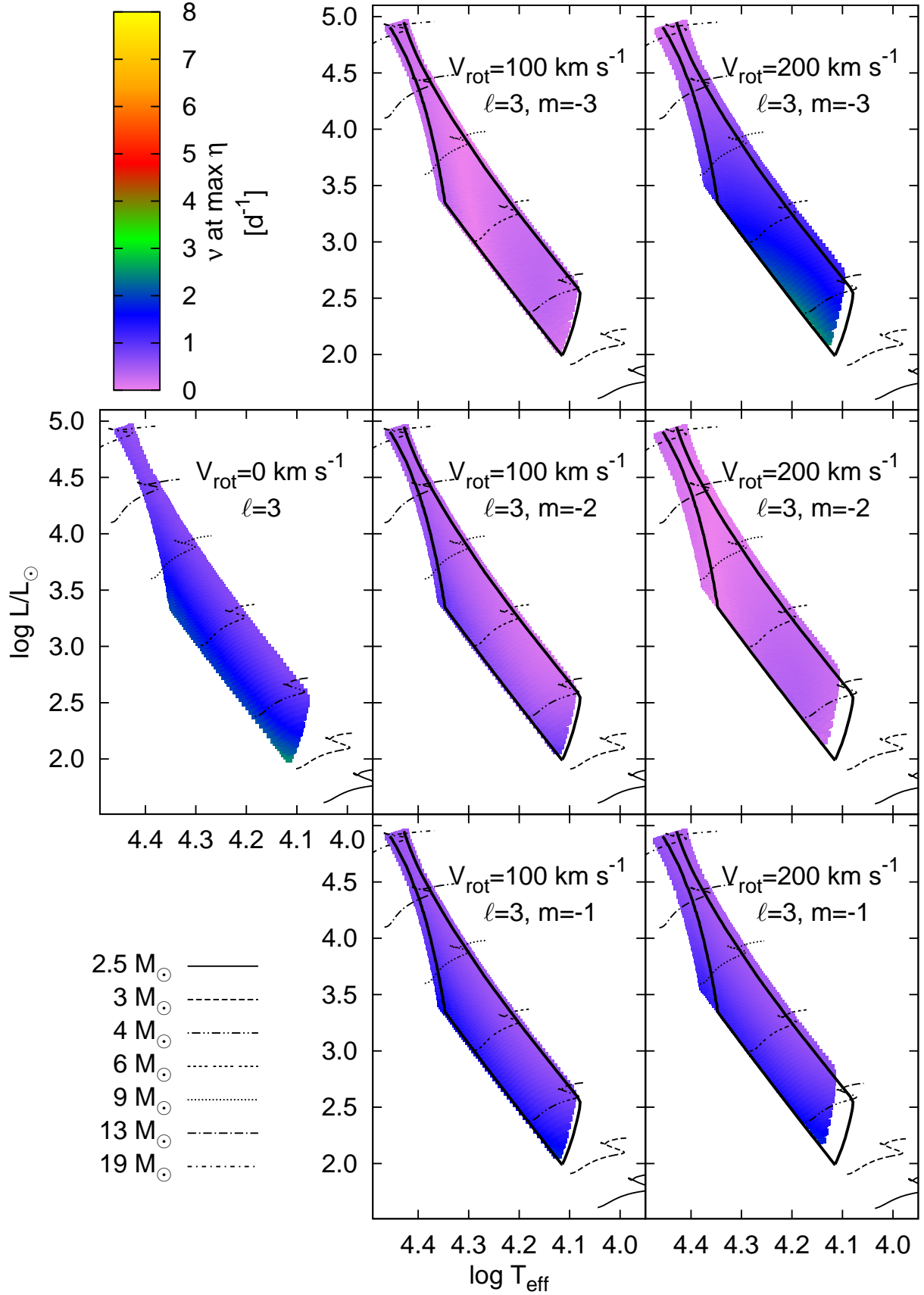


Figure B1. The same as in Fig. 2 but for modes with $\ell = 3$ and $m \leq -1$.

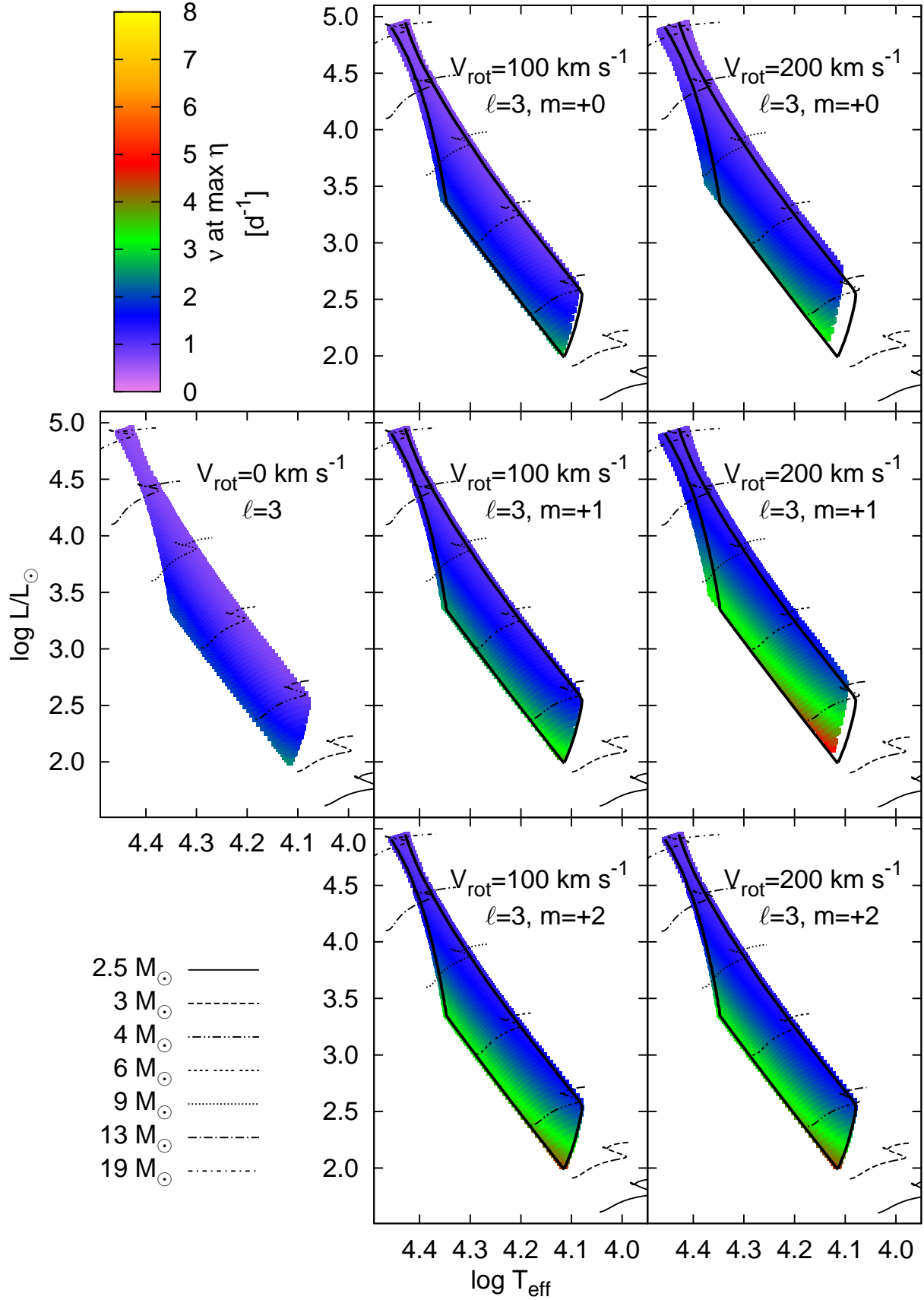


Figure B2. The same as in Fig. 2 but for modes with $\ell = 3$ and $0 \leq m \leq 2$.

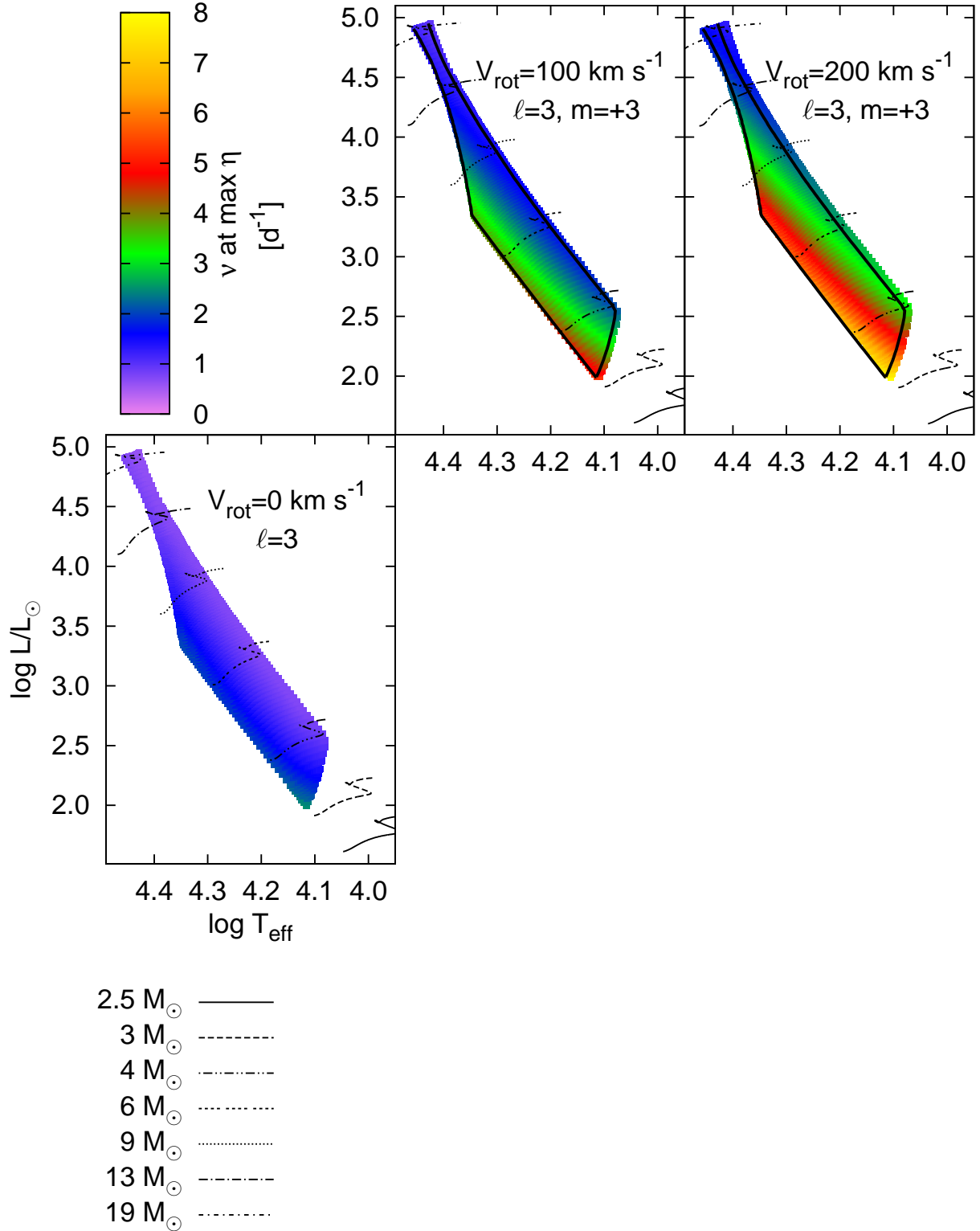


Figure B3. The same as in Fig. 2 but for modes with $\ell = 3$ and $m = 3$.

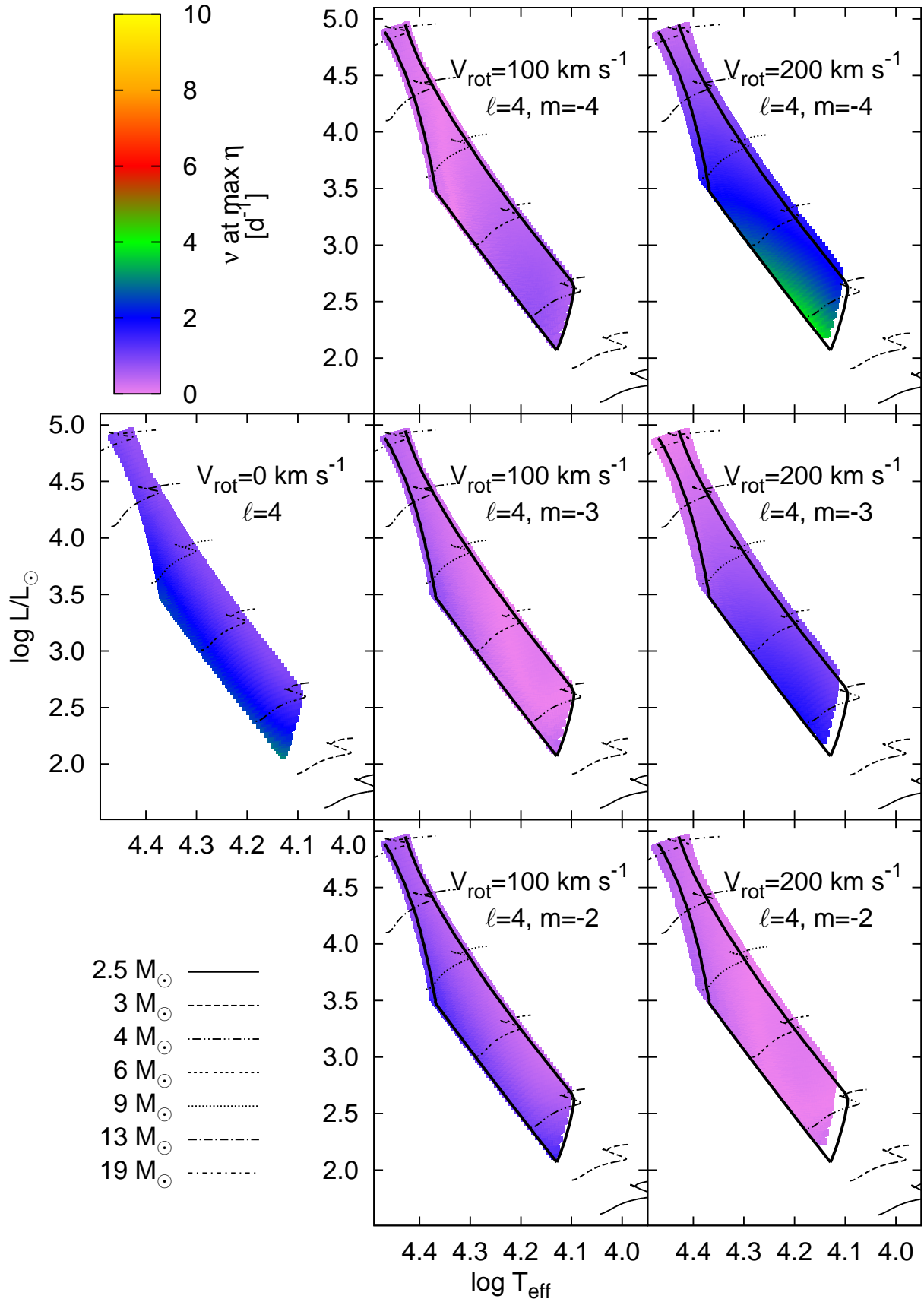


Figure B4. The same as in Fig. 2 but for modes with $\ell = 4$ and $m \leq -2$.

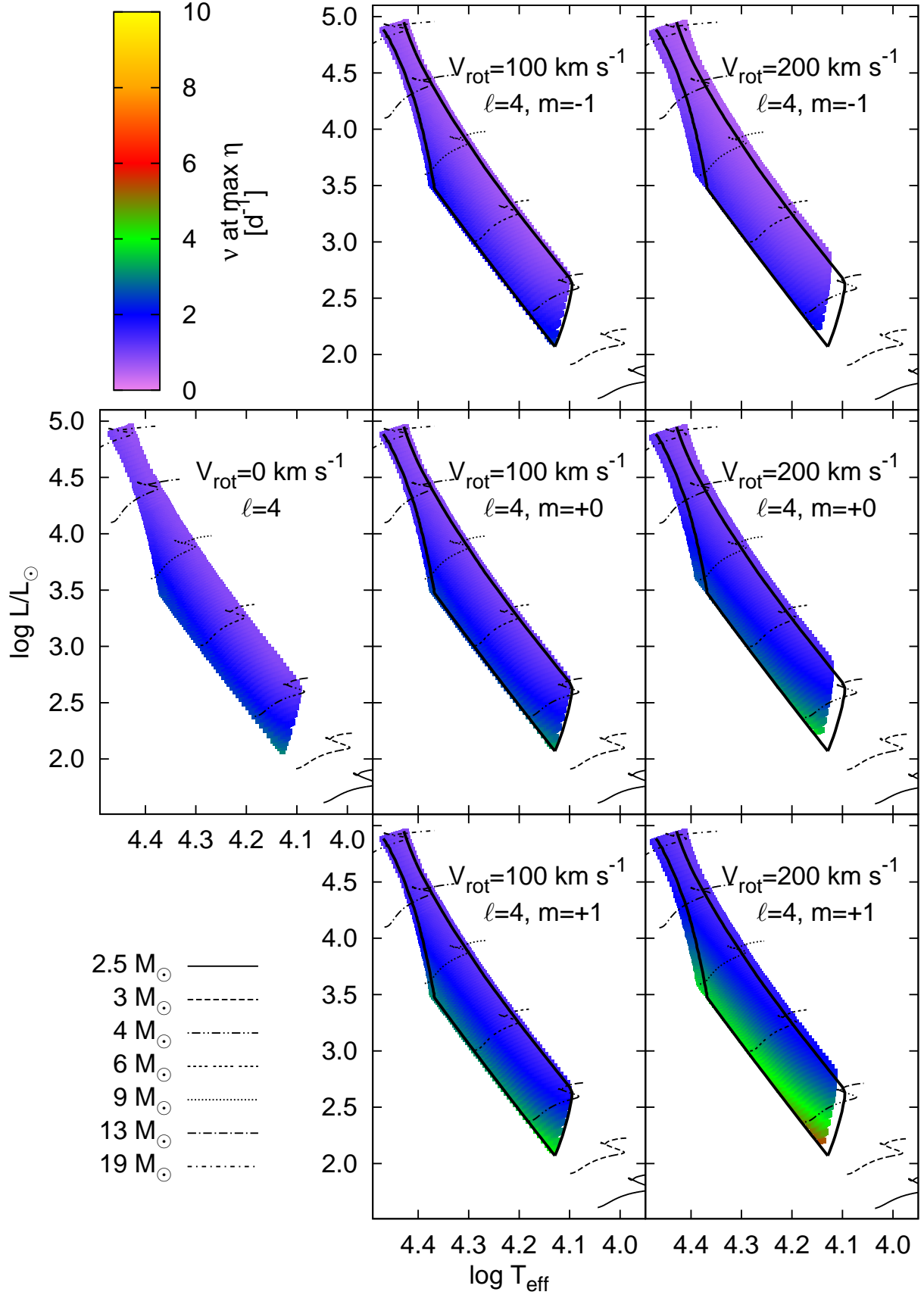


Figure B5. The same as in Fig. 2 but for modes with $\ell = 4$ and $-1 \leq m \leq +1$.

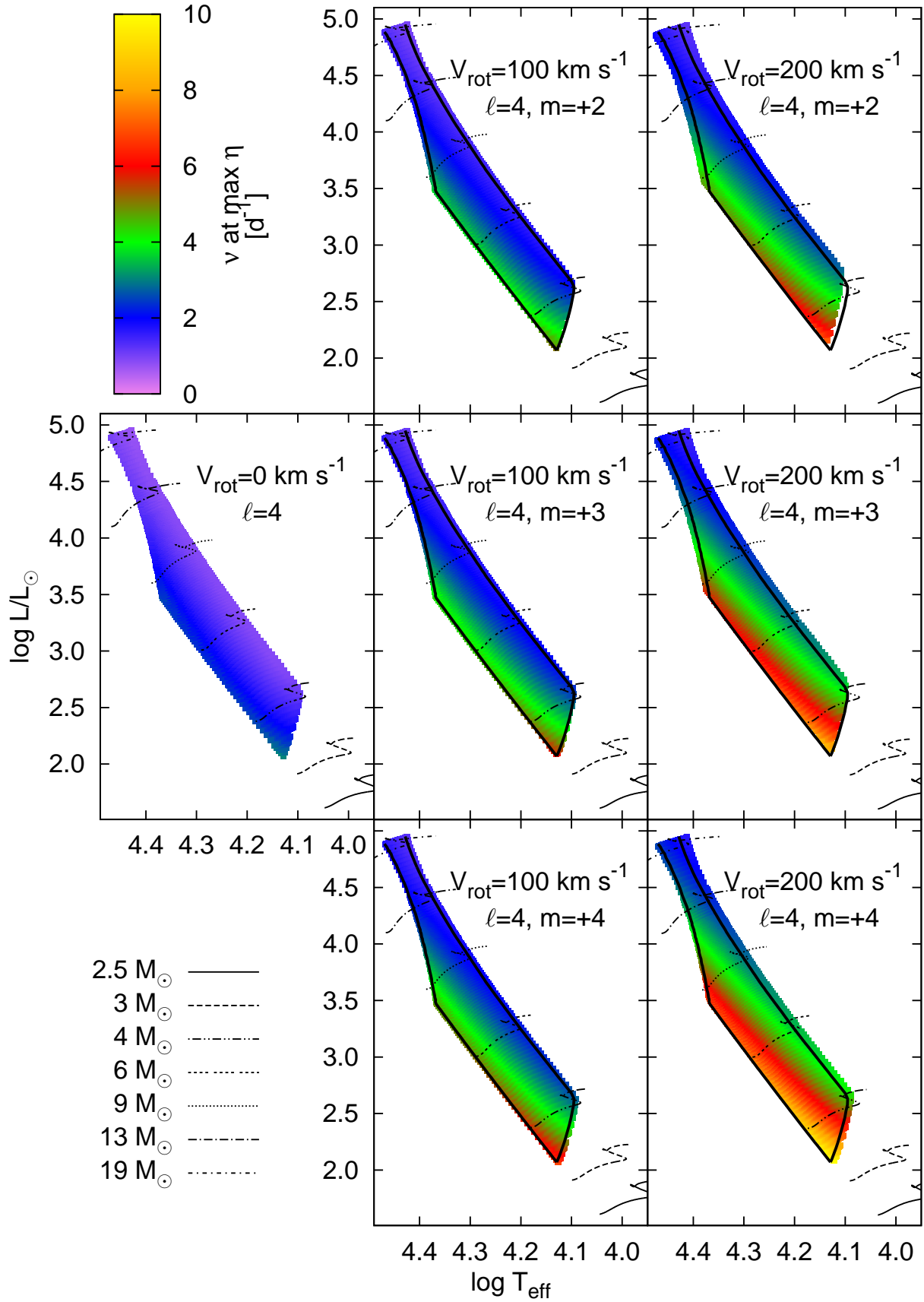


Figure B6. The same as in Fig. 2 but for modes with $\ell = 4$ and $m \geq +2$.

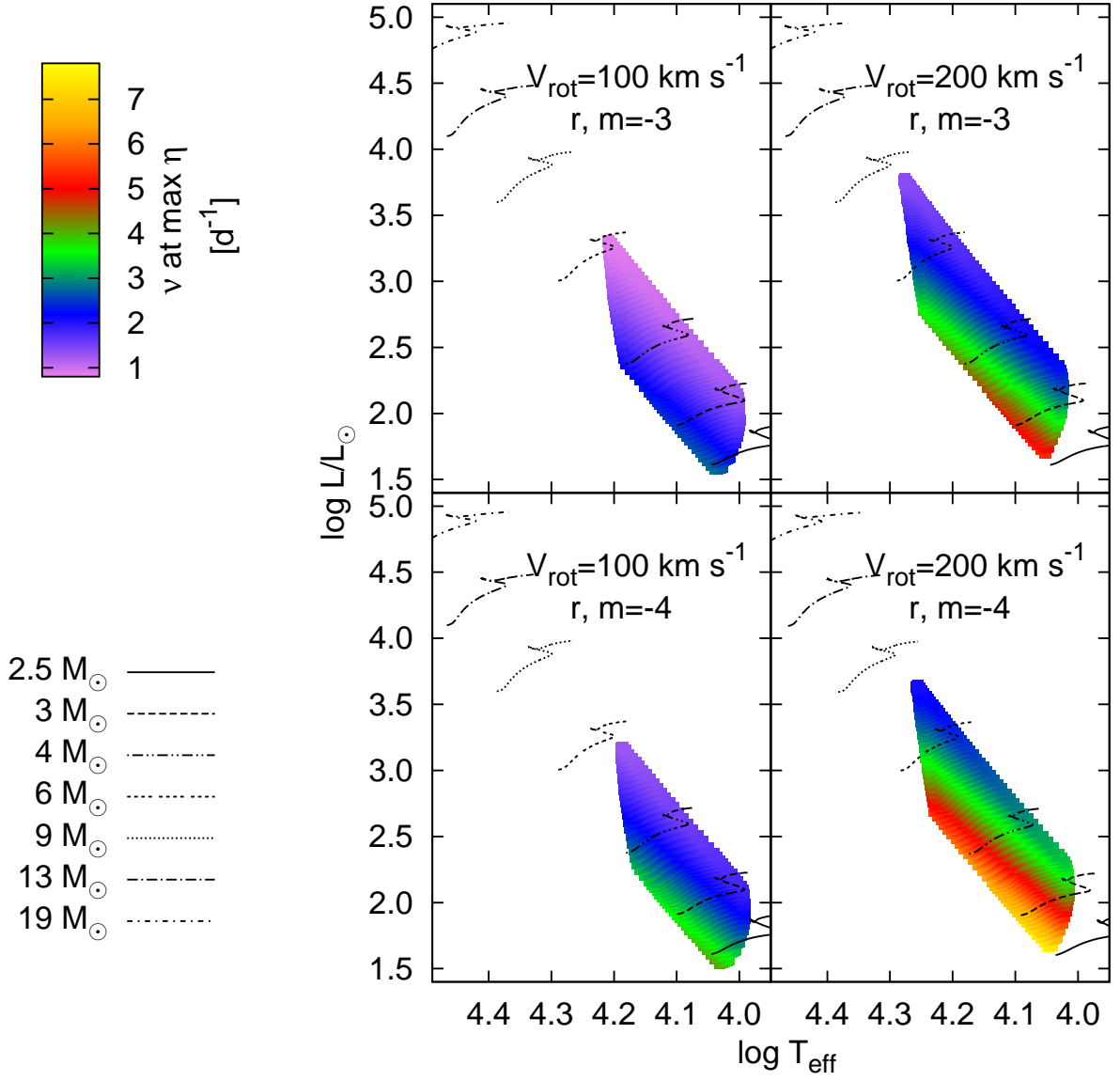


Figure B7. The same as in Fig. 2 but for $r, m = -3, -4$ modes and $V_{\text{rot}} = 100$ and 200 km s^{-1} .

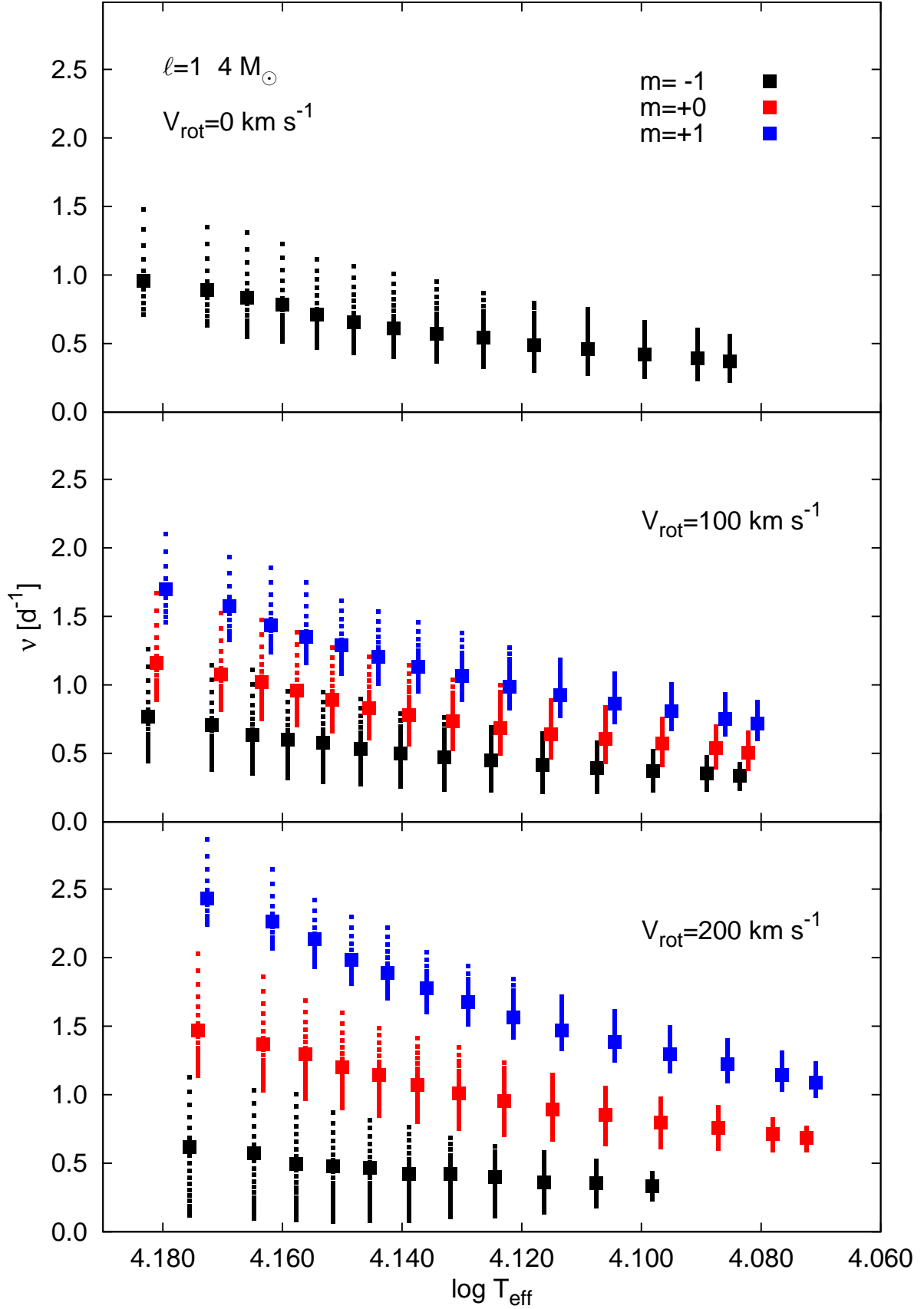
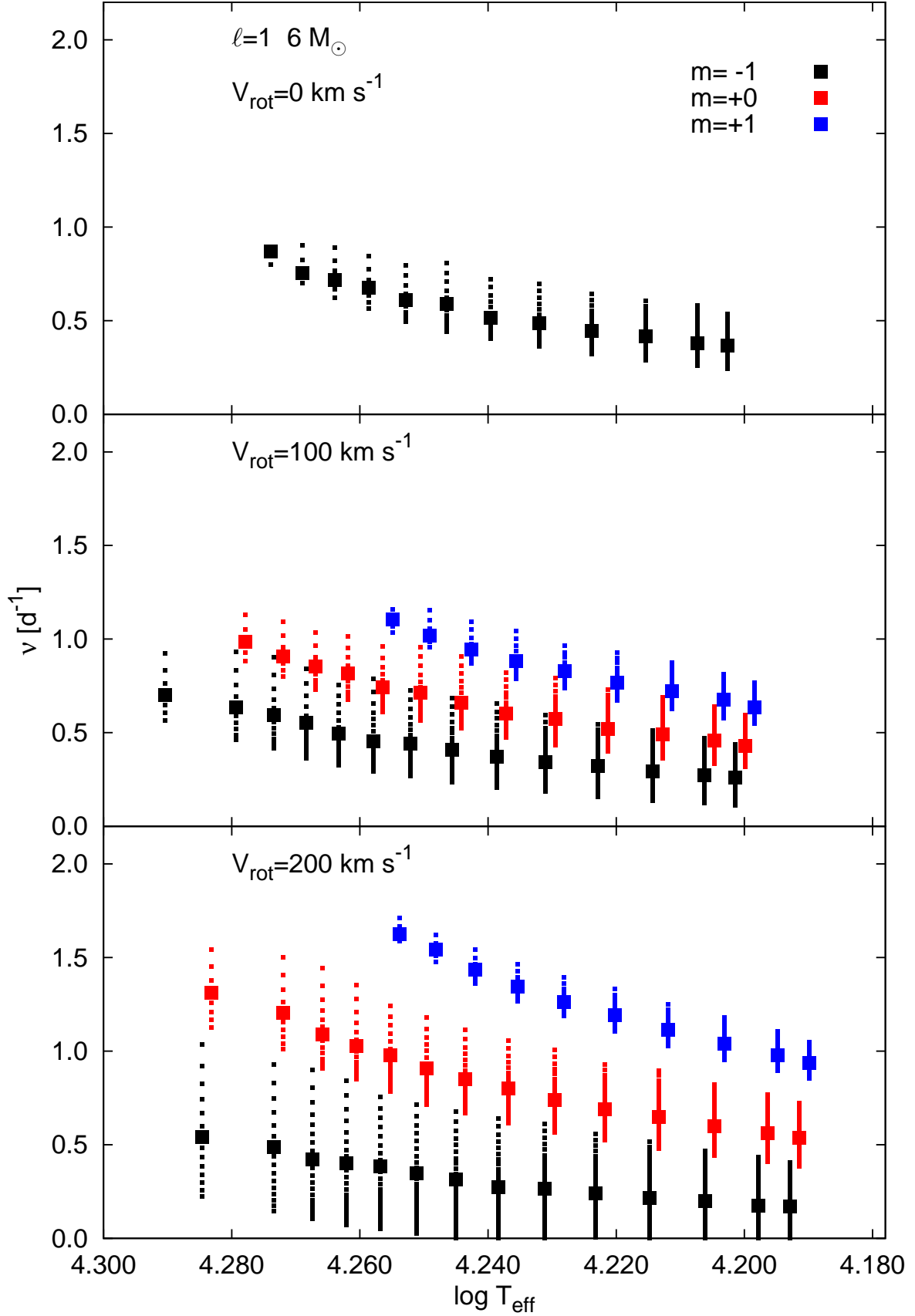


Figure C1. Evolution of the frequencies of unstable dipole modes in a $4 M_{\odot}$ model for three values of rotation velocity. Frequencies corresponding to modes with the maximum values of the instability parameter η are indicated by large symbols.


 Figure C2. The same as in Fig. C1 but for $6 M_{\odot}$ model.

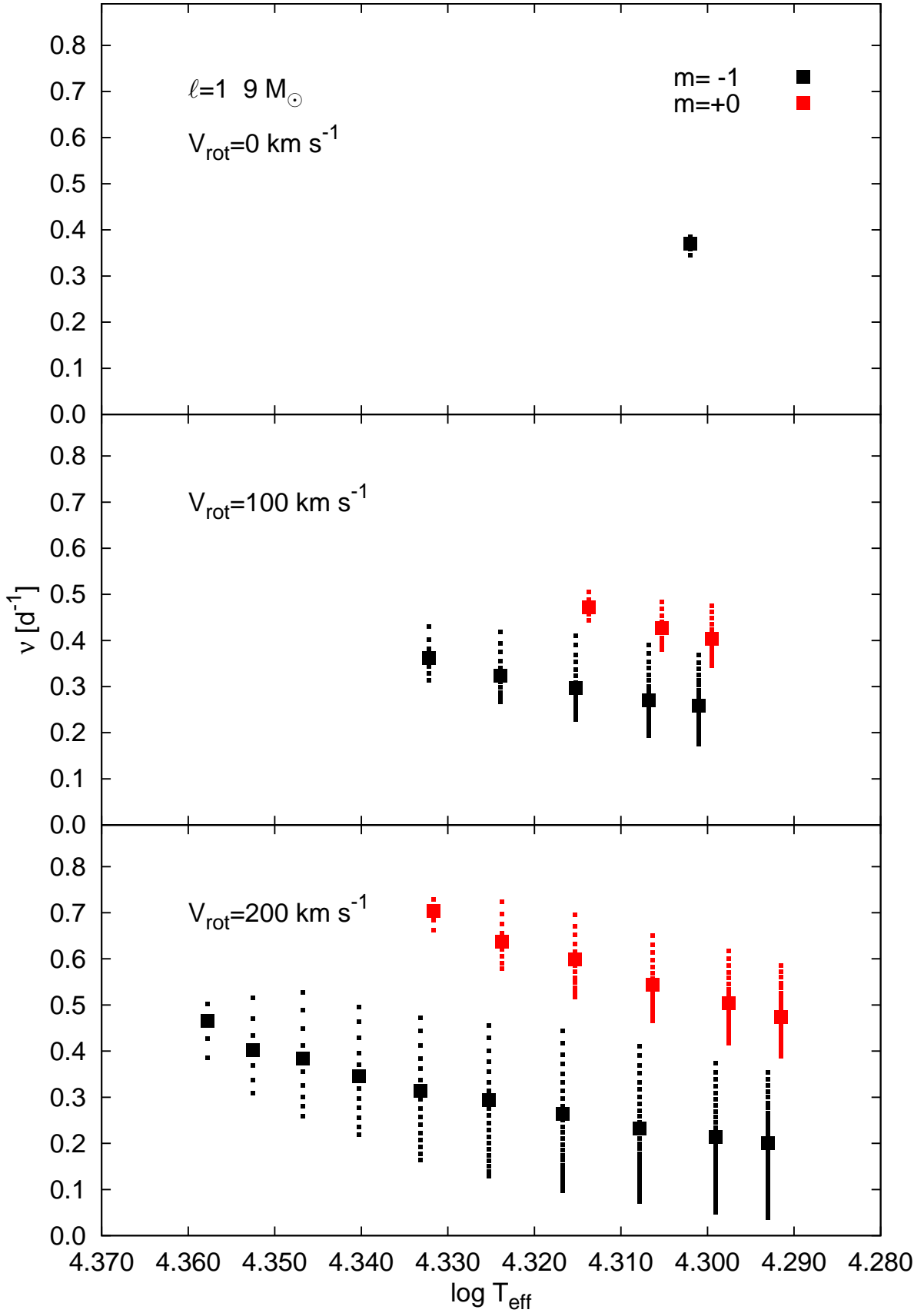


Figure C3. The same as in Fig. C1 but for $9 M_{\odot}$ model.

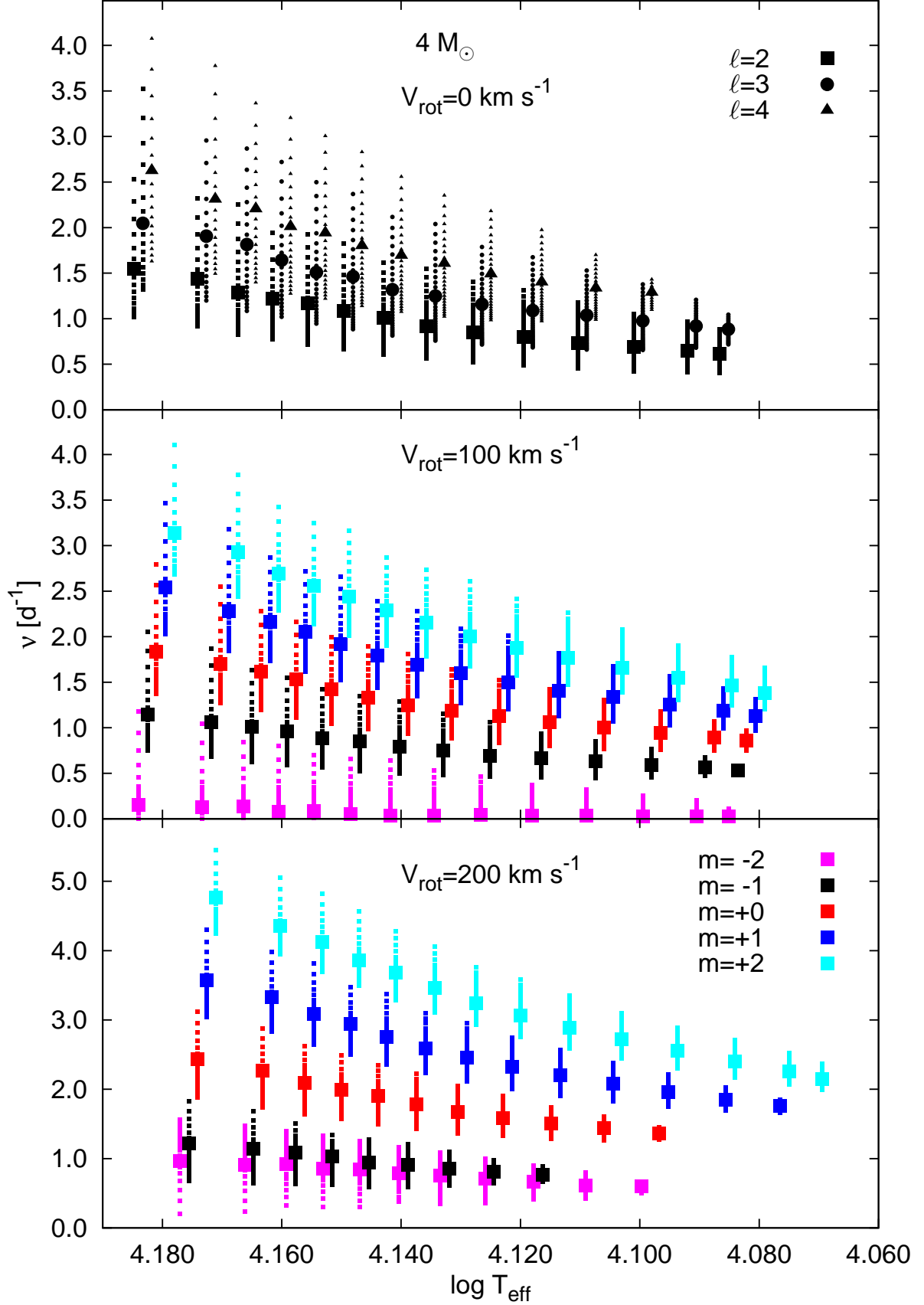


Figure C4. The same as in Fig. C1 but for $\ell = 2 - 4$ in the non-rotating models (the upper panel) and for $\ell = 2$ in the rotating models with the rotation velocity $V_{\text{rot}} = 100 \text{ km s}^{-1}$ (the middle panel) and $V_{\text{rot}} = 200 \text{ km s}^{-1}$ (the bottom panel).

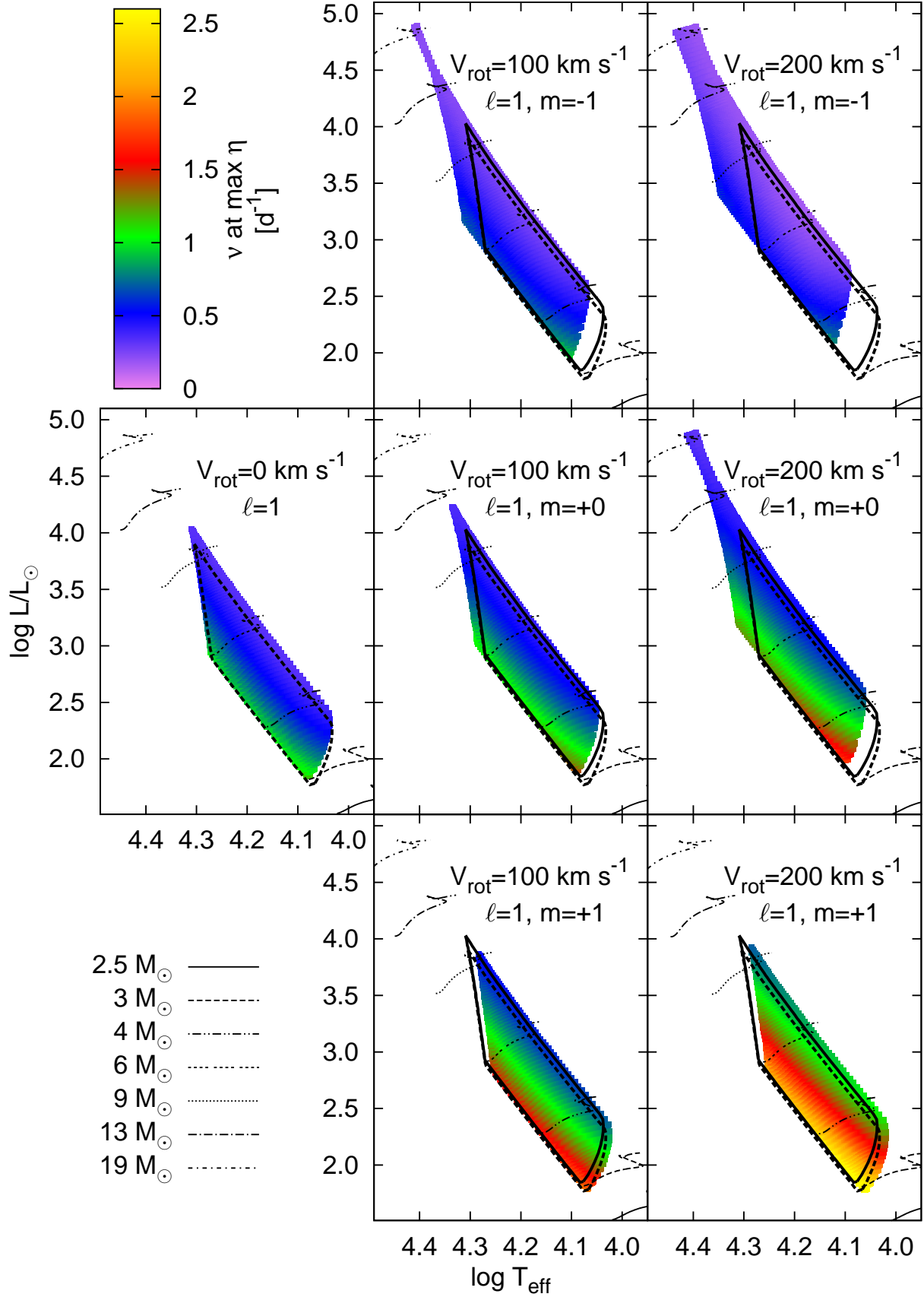


Figure D1. The same as in Fig. 2 but for $X_0 = 0.75$. In addition, we marked the instability strips computed for non-rotating models with $X_0 = 0.70$ (thick dashed line) and $X_0 = 0.75$ (thick solid line).

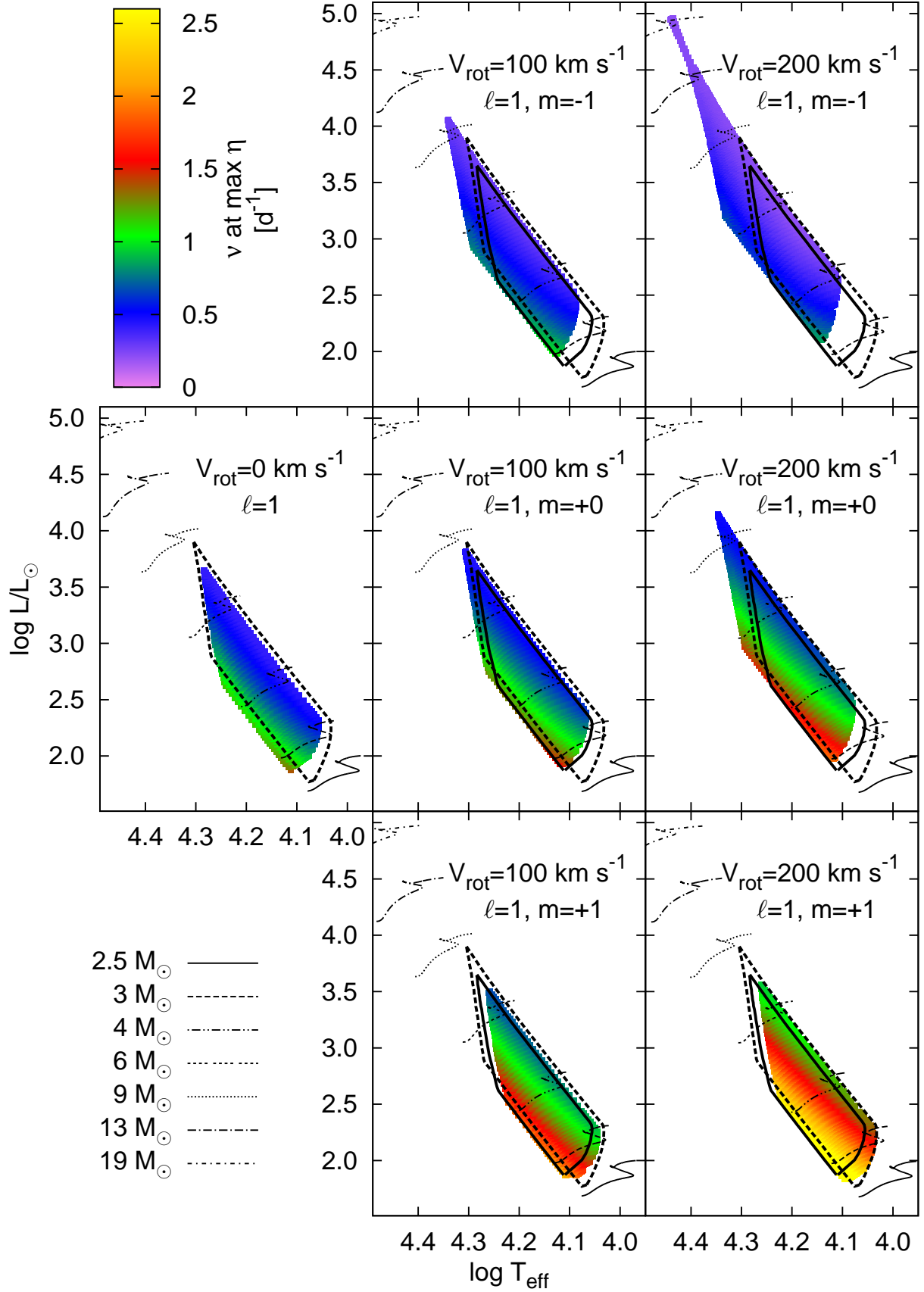


Figure D2. The same as in Fig. D1 but for $Z = 0.010$. In addition, we marked the instability strips computed for non-rotating models with $Z = 0.015$ (thick dashed line) and $Z = 0.010$ (thick solid line).

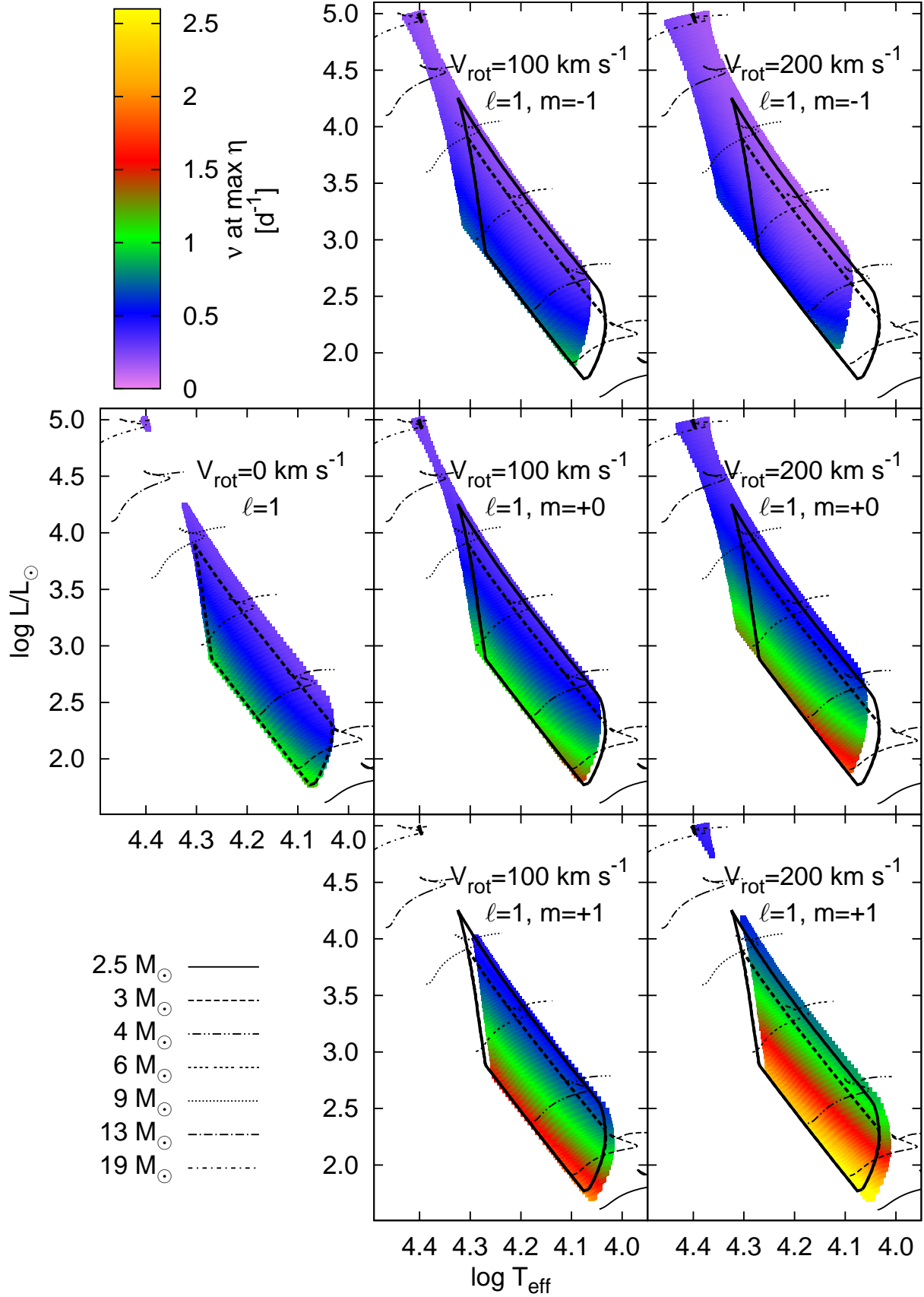


Figure D3. The same as in Fig. D1 but for $\alpha_{\text{ov}} = 0.2$. In addition, we marked the instability strips computed for non-rotating models with $\alpha_{\text{ov}} = 0.0$ (thick dashed line) and $\alpha_{\text{ov}} = 0.2$ (thick solid line).

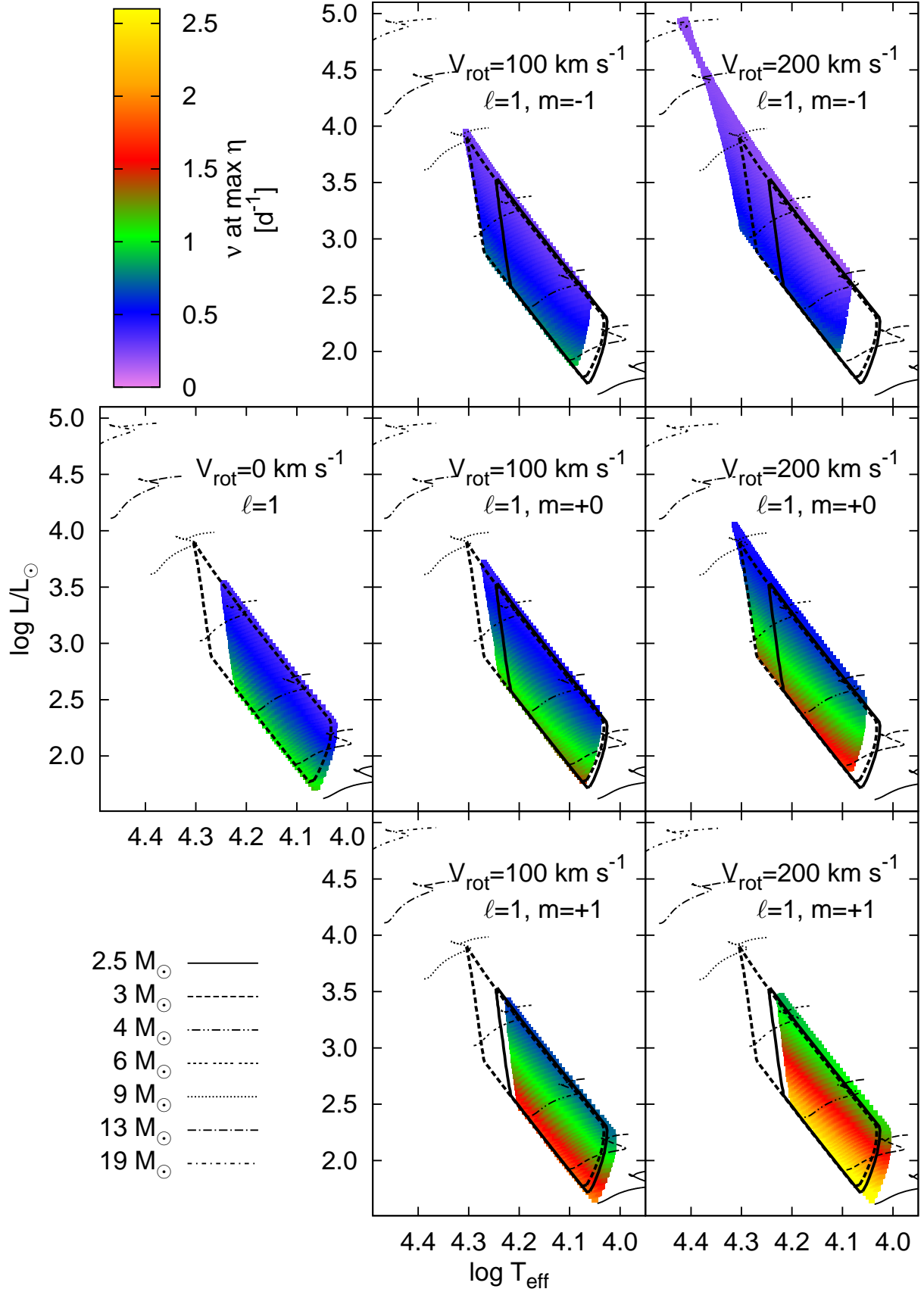


Figure D4. The same as in Fig. D1 but for the OPAL opacity tables. In addition, we marked the instability strips computed for non-rotating models with the OP tables (thick dashed line) and the OPAL tables (thick solid line).

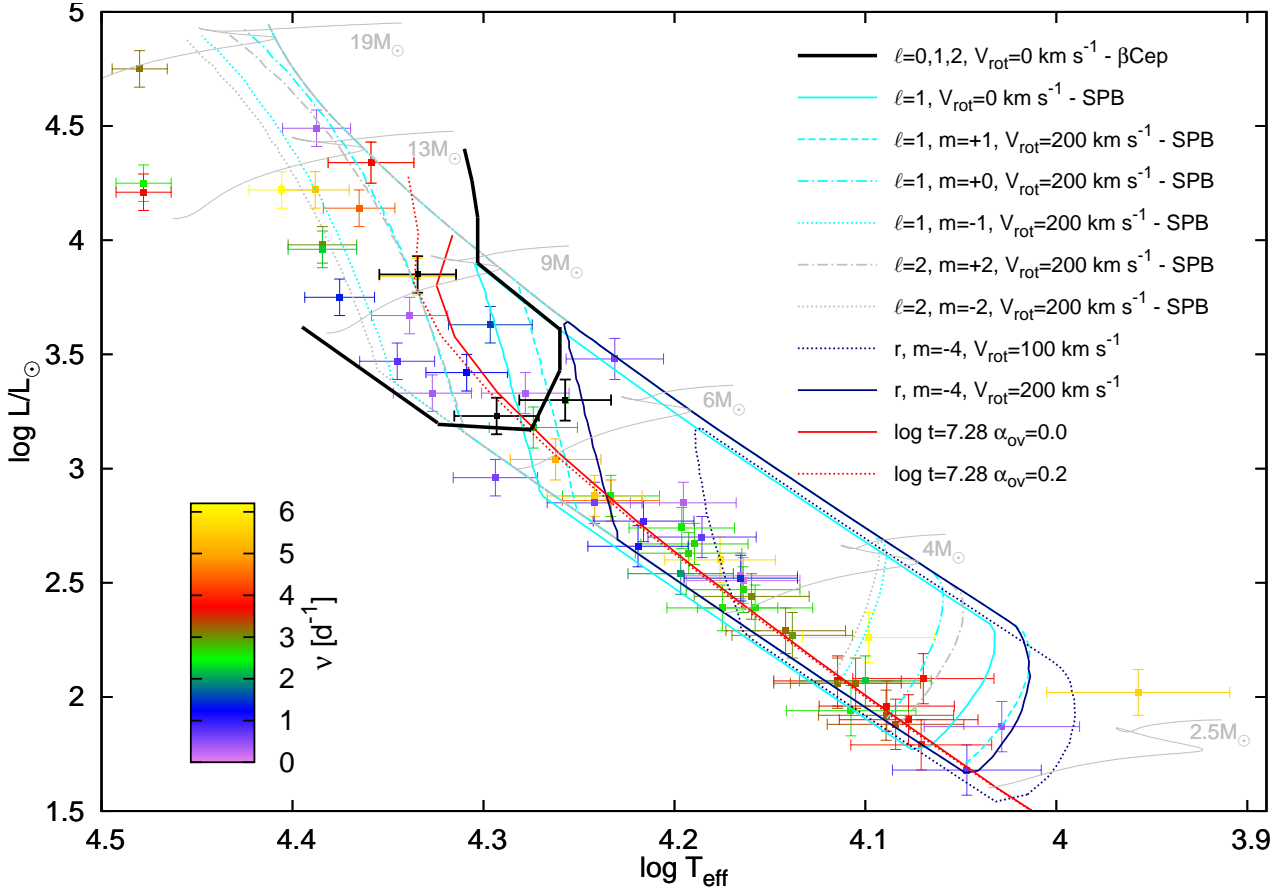


Figure E1. Variable stars observed in NGC 884 (Saesen et al. 2010, 2013). Colours code the frequency of the dominant mode. For clarity, stars with frequencies above 6.3 d^{-1} are marked in black. High-order g modes instability strips for dipole modes excited in non-rotating and in rotating models are enclosed by cyan lines, high-order g modes instability strips for some quadrupole modes excited in rotating models are enclosed by grey lines and instability strips for the $r, m = -4$ modes are enclosed by navy-blue lines. The cool border of the β Cephei instability strip for $\ell = 0, 1, 2$ and non-rotating models is marked by the black continuous line. In addition, there are shown the isochrones corresponding to the maximum age of the cluster, $\log(t/\text{yr}) = 7.28$ (Saesen et al. 2013) for rotating models, $V_{\text{rot}} = 200 \text{ km s}^{-1}$, without overshooting from convective core (red continuous line) and with overshooting from convective core (red dotted line). Some evolutionary tracks calculated with $V_{\text{rot}} = 200 \text{ km s}^{-1}$ and $\alpha_{\text{ov}} = 0.0$ are shown as well.